REVIEW

Freestanding MXene-based macroforms for electrochemical energy storage applications

Qiongqiong Lu[1] 🟢 | Congcong Liu[2] | Yirong Zhao[2,3] | Wengao Pan[1] | Kun Xie[1] | Pengfei Yue[1] | Guoshang Zhang[1] | Ahmad Omar[2] | Lixiang Liu[4] | Minghao Yu[5] | Daria Mikhailova[2]

[1]Institute of Materials, Henan Key Laboratory of Advanced Conductor Materials, Henan Academy of Sciences, Zhengzhou, Henan, China

[2]Leibniz Institute for Solid State and Materials Research (IFW) Dresden e.V., Dresden, Germany

[3]School of Physical Science and Technology, Lanzhou University, Lanzhou, China

[4]School of Engineering, Westlake University, Hangzhou, Zhejiang, China

[5]Faculty of Chemistry and Food Chemistry & Center for Advancing Electronics Dresden, Technische Universität Dresden, Dresden, Germany

Correspondence
Qiongqiong Lu, Institute of Materials, Henan Key Laboratory of Advanced Conductor Materials, Henan Academy of Sciences, Zhengzhou, Henan 450046, China.
Email: qiongqiong.lu@hotmail.com

Minghao Yu, Faculty of Chemistry and Food Chemistry & Center for Advancing Electronics Dresden, Technische Universität Dresden, Dresden 01062, Germany.
Email: minghao.yu@tu-dresden.de

Abstract

Freestanding MXene-based macroforms have gained significant attention as versatile components in electrochemical energy storage applications owing to their interconnected conductive network, strong mechanical strength, and customizable surface chemistries derived from MXene nanosheets. This comprehensive review article encompasses key aspects related to the synthesis of MXene nanosheets, strategies for structure design and surface medication, surface modification, and the diverse fabrication methods employed to create freestanding MXene-based macroform architectures. The review also delves into the recent advancements in utilizing freestanding MXene macroforms for electrochemical energy storage applications, offering a detailed discussion on the significant progress achieved thus far. Notably, the correlation between the macroform's structural attributes and its performance characteristics is thoroughly explored, shedding light on the critical factors influencing efficiency and durability. Despite the remarkable development, the review also highlights the existing challenges and presents future perspectives for freestanding MXene-based macroforms in the realms of high-performance energy storage devices. By addressing these challenges and leveraging emerging opportunities, the potential of freestanding MXene-based macroforms can be harnessed to enable groundbreaking advancements in the field of energy storage.

KEYWORDS
batteries, electrochemical energy storage, freestanding macroforms, MXenes, supercapacitors

1 | INTRODUCTION

Toward a more sustainable future, the development of renewable energy sources (solar, wind, etc.) for electric generation is essential to address the issues of climate change and environmental pollution induced by the overuse of fossil fuels.[1] However, these renewable energy sources are intermittent, thus energy storage devices are needed to balance the electric generation and demand.[2] Among energy storage devices, electrochemical energy storage devices (batteries and supercapacitors) are considered reliable power sources for portable electronics, hybrid vehicles, and smart grids.[3] Lithium-ion batteries (LIBs) represent a widely used energy storage solution, with the merits of non-memory and high energy density.[4] However, the rising cost of lithium-related materials makes it essential to develop other batteries with low cost and high material sustainability. Non-Li batteries (batteries based on Na^+, K^+, Zn^{2+}, Mg^{2+}, Ca^{2+}, and Al^{3+}) have attracted intensive attention as promising low-cost and high-energy technology alternatives for LIBs, particularly in large-scale energy storage applications.[5–9] However, these batteries suffer from low ionic migration kinetics due to the large ionic radius, leading to inferior electrochemical performance.[10] Therefore, it is necessary to develop new electrode materials with high capacity and high rate capability. In addition, supercapacitors store charges through physical ion absorption or redox reactions on the electrode surface. Compared with rechargeable batteries, supercapacitors are featured by high-power density, long operation life, and wide operating temperature range. Electrode materials of supercapacitors with high surface areas and abundant redox sites are highly desired.[11] Freestanding macroforms as electrodes with interconnected and conductive structures are favored for high electrochemical performance. It avoids the use of metal current collectors, non-conductive binders, and non-active additional conductive carbon, enabling high energy densities of the whole electrode.[12–15] Moreover, the robust, and interconnected network of freestanding macroforms can work as conductive host to accommodate the volume change of other active materials, such as sulfur and lithium metal.[16,17]

MXenes, a large family of two-dimensional (2D) materials, were commonly synthesized by selectively etching the A-layers (group IIIA or IVA species) of the MAX phase precursor, where M and X stand for transition metals (Ti, Nb, V, etc.) and carbon or/and nitrogen, respectively.[18,19] They have the chemical formula of $M_{n+1}X_nT_x$ ($n = 1–4$), where T represents termination groups (–F, –O, –OH, etc.) on the surface of the outer M layer.[20] For instance, the first Ti_3C_2 MXene was synthesized from Ti_3AlC_2 by selectively etching the Al layer using the hydrofluoric acid (HF) solution

in 2011 by Gogotsi and coworkers.[21] Since then, various MXenes with different M elements and varying termination groups have been obtained. MXenes possess excellent electron conductivity due to free electrons from transition metals.[22] For example, $Ti_3C_2T_x$ can reach a conductivity of up to 20 000 S cm^{-1}.[23] The abundant surface termination groups of MXenes can work as numerous active sites for redox reactions or metal ions/polysulfide adsorption in batteries and supercapacitors.[24] Besides, MXene nanoflakes can be homogeneously dispersed in water and organic solvents due to their favorable hydrophilic and negatively charged surfaces, which further allow facile fabrication of freestanding MXene architectures (1D fiber/yarn, 2D film, 3D foam) by various approaches, such as vacuum-assisted filtration, spinning, and freeze-drying.[25,26]

Freestanding MXene macroforms are of particular interest for electrochemical energy storage applications, owing to their high electronic conductivity, robust interconnected network, and abundant surface termination groups on MXene flakes. The freestanding MXene film was normally simply fabricated by vacuum-assisted filtration and following drying benefiting from the high aspect ratio and strong interflake interaction of MXenes.[27] Due to the fast electron transport, excellent ion storage capability, and robust interconnected network, freestanding MXene architectures can be straightforwardly used as the electrode for high-performance batteries and supercapacitors without using binders and metal current collectors. In addition, freestanding MXene architectures, benefiting from the robust structure, high electronic conductivity, and functional surface groups, can act as functional scaffolds or current collectors for active materials (sulfur, Li metal, etc.).[28–30] More importantly, different formats of freestanding MXene architectures (1D fiber/yarn, 2D film, 3D foam) show a promising potential application in flexible energy devices with various configurations (fiber/yarn structure, planar structure).[26,31–33]

While previous reviews have explored the application of MXenes in energy storage, there remains a noticeable gap in dedicated reviews specifically focusing on MXene-based macroforms. To address this gap, this compressive review article provides an extensive overview of MXene-based macroforms in context of energy storage (Figure 1).[24,34–44] It covers various aspects including synthesis techniques, structure design, surface chemistry modification, and fabrication methods employed for MXene-based macroforms. Furthermore, the review delves into recent advancements concerning the utilization of MXene-based macroforms as electrode in metal-ion batteries and supercapacitors, as well as their role as hosts for sulfur and metal anodes. By categorizing the applications of MXene-based macroforms based on their specific functions, this review offers
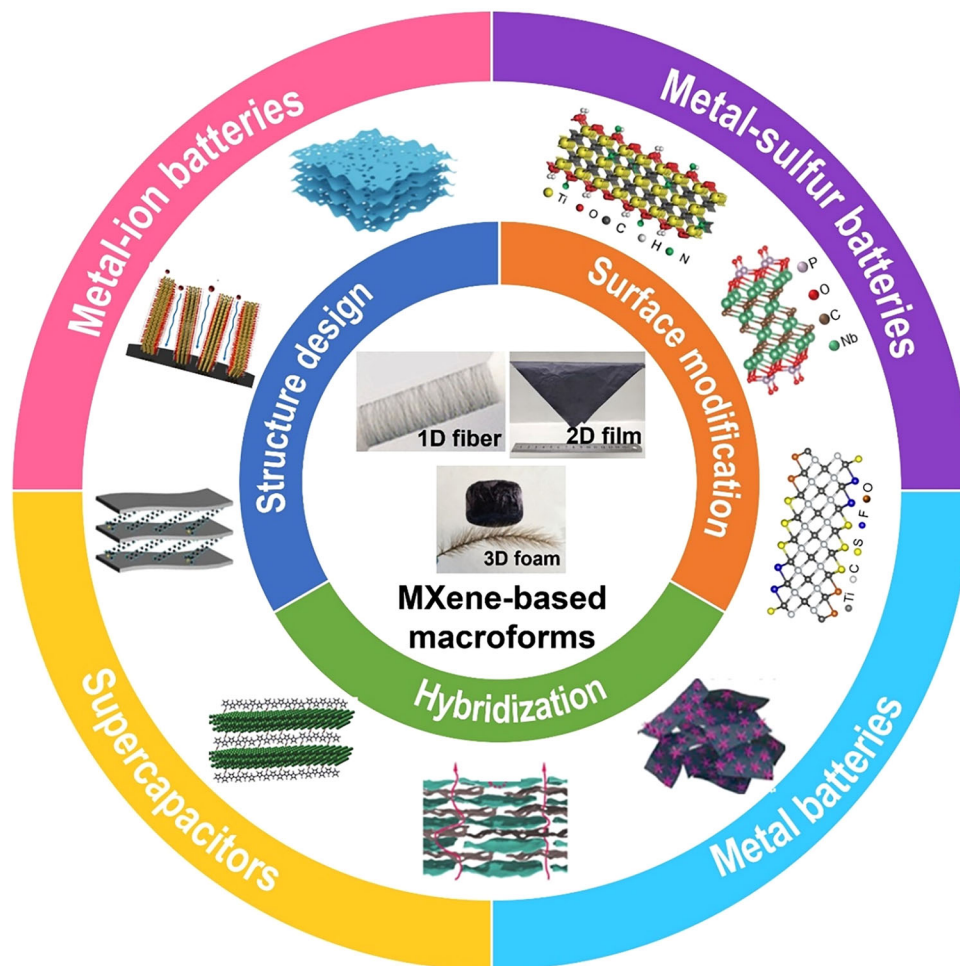
FIGURE 1 Schematic of various strategies for modifying MXene-based macroforms (1D fiber, 2D film, 3D foam), including structure design, surface modification, and hybridization, along with their application in batteries and supercapacitors. 1D Ti_3C_2 fiber. Reproduced with permission.[34] Copyright 2020, American Chemical Society. 2D $Ti_3C_2T_x$ film. Reproduced with permission.[35] Copyright 2021, Wiley-VCH. 3D $Ti_3C_2T_x$ foam. Reproduced with permission.[36] Copyright 2019, Royal Society of Chemistry. Cetyltrimethylammonium bromide (CTAB) pre-pillaring Ti_3C_2 MXene. Reproduced with permission.[37] Copyright 2017, American Chemical Society. Vertical aligned $Ti_3C_2T_x$ MXene films. Reproduced with permission.[38] Copyright 2018, Springer Nature. Porous $Ti_3C_2T_x$ MXene foam. Reproduced with permission.[39] Copyright 2020, Elsevier. $Ti_3C_2T_x$ with –O and –N functional groups. Reproduced with permission.[40] Copyright 2020, Royal Society of Chemistry. Nb_4C_3 with –PO_2 groups. Reproduced with permission.[24] Copyright 2022, Wiley-VCH. S-doped $Ti_3C_2T_x$. Reproduced with permission.[41] Copyright 2019, Wiley-VCH. Sb_2S_3/Ti_3C_2. Reproduced with permission.[42] Copyright 2020, American Chemical Society. $Ti_3C_2T_x$/rHGO film. Reproduced with permission.[43] Copyright 2018, Wiley-VCH. Polypyrrole-$Ti_3C_2T_x$ Reproduced with permission.[44] Copyright 2015, Wiley-VCH. rHGO, reduced holey graphene oxide.

valuable insights into their diverse uses within energy storage systems. Notably, the review emphasizes the correlation between the structure of macroforms and their overall performance, underscoring the critical relationship between the two factors. In addition to discussing the progress achieved thus far, the review also addresses the existing challenges and provides perspectives on the future prospects of freestanding MXene-based macroforms in high-performance energy storage devices. By identifying and highlighting the obstacles that need to be overcome, as well as outlining potential avenues for future research and development, this review aims to inspire future advance-

ments in the field of MXene-based macroforms for energy storage applications.

2 | SYNTHESIS AND PROCESSING OF MXENES

2.1 | Synthesis of MXenes

In general, the synthesis of MXenes can be categorized into two strategies, top–down and bottom–up approaches.[21,45–47] In the top–down strategy, wet chemical etching
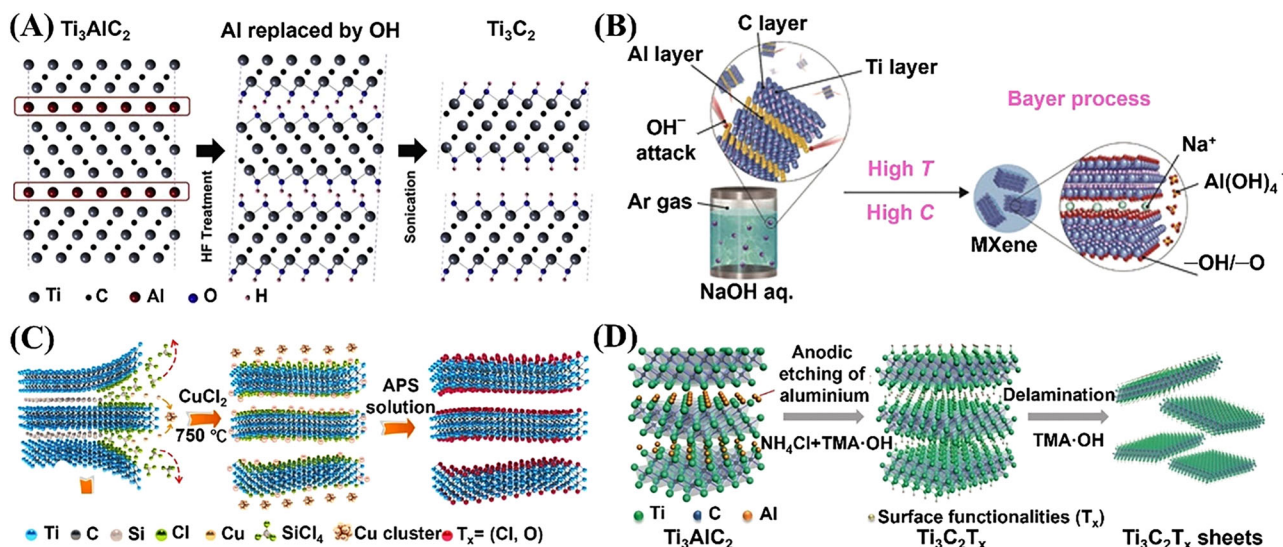
FIGURE 2 (A) Schematic illustration showing the preparation of Ti_3C_2 via the HF treatment. Reproduced with permission.[21] Copyright 2011, Wiley-VCH. (B) Schematic illustration showing the synthesis of $Ti_3C_2T_x$ by the alkali etching method. Reproduced with permission.[45] Copyright 2018, Wiley-VCH. (C) Schematic illustration showing the preparation of $Ti_3C_2T_x$ by the molten salt method. Reproduced with permission.[46] Copyright 2020, Springer Nature. (D) Schematic illustration showing the fabrication of $Ti_3C_2T_x$ through the electrochemical etching approach. Reproduced with permission.[47] Copyright 2018, Wiley-VCH.

is commonly used, including F-containing strong acid etching, alkali etching, and electrochemical etching.[48–50] Taking the most studied Ti_3C_2 MXene as an example, accordion-like Ti_3C_2 was obtained by immersing Ti_3AlC_2 into 50% concentrated hydrofluoric acid for 2 h at room temperature to selectively etch the Al layer (Figure 2A).[21] The exposed surface Ti layer of Ti_3C_2 was terminated by functional groups of –OH, –O, and –F. Following a similar etching method, various MXenes were synthesized, such as $Nb_{1.33}CT_x$,[51] $Ta_4C_3T_x$,[52] Mo_2CT_x,[53] V_2CT_x,[54] Nb_2CT_x,[55] $W_{1.3}CT_x$,[56] $Zr_3C_2T_x$,[57] and Hf_3C_2.[58]

The hazardous concentrated hydrofluoric acid can be replaced by milder etching agents such as fluoride salt or the strong acid and fluoride salt mixture.[59,60] Ghidiu et al.[59] adopted LiF-added 6 M HCl to etch Ti_3AlC_2 at 40°C for 45 h. The resultant $Ti_3C_2T_x$ showed a larger lateral size of up to 0.5–1.5 μm, a particle tightly stacked morphology, and a clay-like paste format. Such clay-like characteristic is ascribed to the intercalation of water and cation between the Ti_3C_2 sheets. Based on this method, other MXenes were also successfully prepared, such as Ti_2NT_x[61] and Mo_2CT_x.[62]

Fluorine-free synthesis methods were developed by employing basic agents. As a representative example, Li et al.[45] applied a NaOH-assisted hydrothermal process for preparing $Ti_3C_2T_x$ (T = –OH, –O). The hydrothermal reaction was conducted using 27.5 M NaOH at 270°C (Figure 2B). High-purity $Ti_3C_2T_x$ (92 wt%) without –F termination was obtained, showing a compact layered structure and a large interlayer spacing of 12 Å due to the intercalation of Na^+.

Another commonly used top–down approach is molten salt etching pioneered by Huang's group.[46,63,64] For example, Huang and coworkers[46] reported that $Ti_3C_2T_x$ MXene with O and Cl terminations was synthesized using the reaction between Ti_3SiC_2 and the Lewis acidic $CuCl_2$ molten salt at 750°C, followed by washing with an ammonium persulfate solution to remove the generated Cu (Figure 2C). This Lewis acidic molten salt approach represents a universal manner to produce a variety of MXenes, such as $Ti_4N_3T_x$[64] and Nb_2CT_x.[65] Moreover, the surface terminations (Br, I, etc.) can be adjusted by using molten salts with different halide anions (Br^-, I^-, etc.).

Electrochemical etching of MAX for the MXene synthesis was also developed by avoiding the use of harsh acid/alkali or molten salt with high-temperature operation.[47,66–68] Li et al.[66] reported that V_2AlC was electrochemically converted into V_2CT_x in an aqueous zinc-ion battery. Specifically, CR2030 coin-type cell was assembled by using V_2AlC as the cathode, Zn metal as the anode, and 21 M LiTFSI and 1 M $Zn(OTf)_2$ as the electrolyte. V_2CT_x with –F and =O/OH terminations was obtained by the reaction between the V_2AlC and F^- from the electrolyte after 400 charge/discharge cycles at 10 A g^{-1}. Yang et al.[47] demonstrated the anodic corrosion of Ti_3AlC_2 in a binary aqueous electrolyte for the synthesis of $Ti_3C_2T_x$ MXene (Figure 2D). The chloride salt was used with the aim to etch Al due to the strong Al–Cl bonding,

TABLE 1 Advantages and disadvantages of different MXene synthesis methods.

Strategy	Method	Advantages	Disadvantages
Top–down synthesis	F-containing acid etching	High efficiency	Hazardous, –F terminals formed
	Alkali etching	Relatively safe, without –F terminal	Harsh reaction condition
	Molten salt etching	High efficiency, terminals controllable	Harsh reaction condition, high temperature required
	Electrochemical etching	High safety	Limited yield for high-quality MXene
Bottom–up synthesis	CVD	High quality, large area, size and thickness controllable	Time consuming, low yield, high temperature required, high cost
	PEPLD	High quality, large area, thickness controllable	Low yield, relative high cost

Abbreviations: CVD, chemical vapor deposition; PEPLD, plasma-enhanced pulsed-laser deposition.

while a NH_4^+ salt was applied for the intercalation into $Ti_3C_2T_x$ to open edges for a highly efficient etching underlying the surface. After further delamination in tetramethylammonium hydroxide (TMAOH), single-layer or few-layer $Ti_3C_2T_x$ (T = O and OH) nanosheets with a high yield (>90%) and large lateral size of up to 18.6 μm were achieved.

Apart from top–down approaches, certain efforts have also been devoted to directly synthesizing MXenes with bottom–up growth strategies, such as chemical vapor deposition (CVD)[69,70] and plasma-enhanced pulsed-laser deposition (PEPLD).[71] For instance, Xu et al.[69] successfully synthesized ultrathin α-Mo_2C with higher quality and a larger size of over 100 μm by a CVD process at a temperature above 1085°C, as compared to defective MXene with a maximum size of ~10 μm fabricated by chemical etching. Recently, Wang et al.[70] synthesized Ti_2CCl_2 by the reaction of $TiCl_4$ and CH_4 on Ti surface using CVD. The formed Ti_2CCl_2 is perpendicular to the Ti, and could buckle off the Ti surface to form vesicles. Besides, Zhang et al.[71] fabricated ultrathin large-area single-crystalline Mo_2C via the PEPLD method at a lower temperature of 700°C. The advantages and disadvantages of different MXene synthesis methods are summarized in **Table 1**.[72]

2.2 | Structure modification of MXenes

MXenes obtained from etching are normally bulk particles consisting of stacked multilayers because of the van der Waals interactions and hydrogen bonds. In this sense, the specific surface area of MXene cannot be fully utilized. To produce few-layers or single-layer MXene nanoflakes, intercalators (organic molecules, cations, etc.) are normally introduced to weaken the interlayer interactions and expand the interlayer. Subsequently, a sonication step is

applied to break the interaction between MXene layers for delamination and the centrifugation step is generally followed to remove traces of unreacted MAX phase and multilayer MXenes (Figure 3A).[49,73] Organic molecules (e.g., dimethyl sulfoxide [DMSO], hydrazine, tetrabutylammonium hydroxide, and TMAOH) can be inserted into MXenes by simple liquid-phase immersion.[74,75] Besides, cations (e.g., Li^+, Na^+, NH_4^+, Mg^{2+}, and Al^{3+}) were also used as intercalators for delamination.[49] However, delaminated MXene sheets are prone to oxidative degradation in oxygen-dissolved water solution. Oxidation was revealed to be edge driven and flake size/temperature dependent (Figure 3B,C). Low-concentration MXene solution with a small MXene flake size is easily oxidized at room temperature. To stabilize the MXene solution, it is preferred to store MXene in an Ar atmosphere and at a low temperature (~5°C).[73]

On the other hand, the obtained MXene nanosheets are prone to self-stacking driven by the van der Waals forces, which would reduce the electrolyte-accessible surface area of MXene and deteriorate the ion transport.[38,39,76,77] Applying templates (e.g., MgO, polymer sphere) is the mostly used strategy to improve the surface area and porosity of freestanding MXene macrofoams.[24,39,76,78,79] For example, Li et al.[76] adopted polystyrene (PS) microspheres with a diameter of 500 nm as the template to fabricate the MXene electrode with a 3D open structure (Figure 4A). The negatively charged PS spheres were homogeneously dispersed in the solution containing positively charged $Ti_3C_2T_x$, and the freestanding film consisting of $Ti_3C_2T_x$-wrapped PS spheres was obtained by a vacuum filtration approach. After removing PS by annealing, the freestanding $Ti_3C_2T_x$ film with a 3D interconnected structure and high electronic conductivity (600 S cm^{-1}) was gained. Although a hard template can improve the open structure of the MXene macroform, diffusion through the MXene plane is
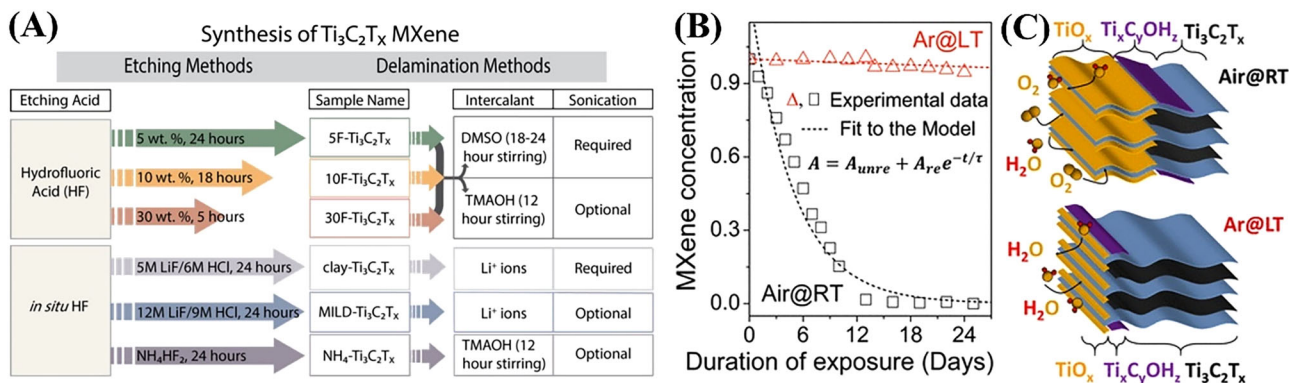
FIGURE 3 (A) Preparation of delaminated $Ti_3C_2T_x$ by various approaches. Reproduced with permission.[49] Copyright 2017, American Chemical Society. (B) Stability and (C) schematic illustration of degradation of the colloidal $Ti_3C_2T_x$ aqueous solution in air at room temperature and in Ar at low temperature (~5°C). Reproduced with permission.[73] Copyright 2017, American Chemical Society.
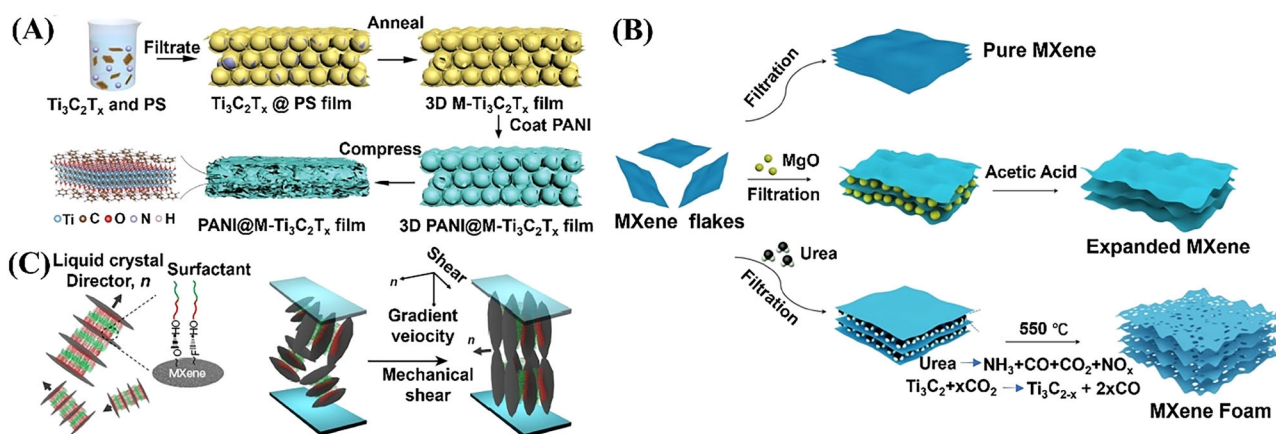
FIGURE 4 (A) Schematic illustration showing the preparation of the compressed PANI@macroporous-$Ti_3C_2T_x$ electrode. Reproduced with permission.[76] Copyright 2019, Wiley-VCH. (B) Synthesis scheme of MXenes in various forms. Reproduced with permission.[39] Copyright 2020, Elsevier 2020. (C) Illustration showing the surfactant ($C_{12}E_6$)-enhanced lamellar structure of the MXene lamellar liquid crystal (MXLLC) and alignment method used. Reproduced with permission.[38] Copyright 2018, Springer Nature. PANI, polyaniline.

still limited to the particle edge pathway. Creating holes on the MXene plane via the etching process is able to improve porosity and thus facilitate ion transport.[39,80] For example, Ren et al.[80] employed a chemical etching method using a transition metal salt (e.g., $CuSO_4$), followed by the acid treatment to produce a porous $Ti_3C_2T_x$ MXene. With the help of catalytic Cu^{2+}, $Ti_3C_2T_x$ MXene flakes were partially oxidized to TiO_2 by the dissolved O_2 in water. After the HF acid treatment, TiO_2 was removed, and pores with tens of nanometers in size were generated on $Ti_3C_2T_x$ MXene flake. In addition, Cui et al.[81] employed cold pressing and annealing treatment in an H_2/Ar atmosphere to produce a freestanding $Ti_3C_2T_x$ MXene film with dense planar macropores, in-plane defects, and expanded interlayer spacings. Benefiting from the well-packed structure of MXene fabricated by cold pressing, the generated gaseous species (TiF_4, CO_2, etc.) were confined within the

space among the MXene nanosheets during the annealing process. Because of gas evolution, macropores and in-plane defects were induced on the MXene flakes. Furthermore, Zhu et al.[39] compared the pristine $Ti_3C_2T_x$ film fabricated by filtration of $Ti_3C_2T_x$ MXene solution, expanded MXene prepared by filtration and acid treatment using MgO with a diameter of 50 nm as the template, and an MXene foam made by filtration and annealing utilizing urea as pore maker (Figure 4B). The MXene/urea film was first fabricated by filtration of the mixture of MXene and urea, and formed CO_2 etched the carbon from MXene generating voids between the MXene nanosheets after pyrolyzing. The obtained MXene foam consisting of curved and porous $Ti_3C_2T_x$ nanosheets, due to the shortened ionic transport pathway, showed the highest efficiency in facilitating the electrolytic ions to enter the whole volume of the MXene electrode.

The strategies of employing templates to increase the interlayer spacing and etching to enhance the porosity are still limited to shortening the long ionic transport paths, because of the non-straight ionic transport pathways. In this sense, vertical alignment of MXene flakes can result in direct ion transport and thus shortened ionic diffusion pathway, thus enabling fast ionic transport. Xia et al.[38] prepared vertically aligned $Ti_3C_2T_x$ nanosheets via mechanical shearing of discotic MXene lamellar liquid crystal (MXLLC) (Figure 4C). MXLLC was induced by relying on the strong hydrogen bonds between −OH groups of hexaethylene glycol monododecyl ether ($C_{12}E_6$) surfactant and −F/−O groups of MXene. The aligned MXLLC formed under a uniaxial in-plane mechanical shear force, enabling directional ion transport and thickness-independent electrochemical performance.

2.3 | Surface modification of MXenes

The surface terminal groups of MXene play a crucial role in the physicochemical properties (e.g., wettability and redox activity) and electrochemical performance.[82–84,85] For example, −F and −OH groups would worsen the ionic transport, while −OH would result in larger interlayer spacing. It is important to regulate terminal groups on the MXene surface for modulating MXene properties. Normally, MXene nanosheets were synthesized using HF or fluoride salt, and the termination groups such as −F, −OH, and −O groups are present. To avoid the negative effect of the −F groups, a fluoride-free synthesis method can be used.

In addition to changing the synthesis method, surface modification can be achieved through annealing or other treatment approaches. Annealing conditions of an MXene film fabricated by cold pressing in an N_2/H_2 atmosphere were investigated by Cui et al.[81] They found out that, compared with pristine MXene, the MXene sample annealed at 500°C presented macropores, less −F and −Cl groups, more −OH terminations, expanded interlayer spacing, and in-plane defect with a size: of 3.22 nm. All these features enabled the annealed MXene sample with superior electrochemical performance in LIBs.

Heteroatom doping (N, S, P, etc.) is the most commonly used manner to modify the MXene surface and improve the electrochemical performance.[24,82–86] For example, Fan et al.[82] fabricated N-doped $Ti_3C_2T_x$ (N-$Ti_3C_2T_x$) using a template route (Figure 5A). The positively charged melamine formaldehyde (MF) nanospheres were applied as both a template and nitrogen source, and they were wrapped by negatively charged MXene nanoflakes driven by the electrostatic attraction when mixing MXene and MF solution. A porous N-$Ti_3C_2T_x$ was obtained after anneal-

ing at 500°C in Ar. Moreover, Lu et al.[83] comprehensively studied nitrogen doping via experimental characterization and density functional theory (DFT) simulation. They found out that, based on formation energies, three possible sites were identified to accommodate the nitrogen dopant, that is, lattice substitution (LS) for carbon, functional substitution (FS) for −OH, and surface absorption (SA) on the −O termination (Figure 5B). Moreover, they synthesized N-doped Ti_3C_2 MXene, and the position of the nitrogen atom was confirmed by X-ray photoelectron spectroscopy analysis. The total capacitance can be divided into the diffusion-controlled part and the capacitor-like part. The diffusion-controlled part is determined by the valence change of the Ti element in Ti_3C_2 MXene, while the capacitor-like part is related to electrical double-layer capacitance and redox reaction from SA and functional groups. LS-type N endows a higher oxidation state of the Ti element due to the bond of Ti and nitrogen at the lattice site, which improved diffusion-controlled part capacitance. On the other hand, FS-type N and SA-type N enhanced the capacitor-like part, which was related to the SA and functional groups. Wei et al.[84] prepared phosphorus-doped MXene by the thermal treatment with sodium hypophosphate as a phosphorus source at 350°C (Figure 5C). P-containing groups (P−O and P−C bonds) were formed in $Ti_3C_2T_x$, and the interlayer spacing of $Ti_3C_2T_x$ was increased from 12.87 to 14.55 Å. Besides, an S, N-doped MXene was fabricated by intercalating thiourea into $Ti_3C_2T_x$, followed by an annealing treatment.[85] Specifically, thiourea-intercalated $Ti_3C_2T_x$ was fabricated by vigorous mechanical mixing of thiourea and a $Ti_3C_2T_x$ solution. After the freeze-drying process, thiourea-intercalated $Ti_3C_2T_x$ was annealed at 500°C under H_2/Ar to obtain N, S-doped $Ti_3C_2T_x$.

2.4 | Hybridization of MXenes

Hybridization is another commonly used strategy to combine the advantages of MXene and guest materials.[87,88] More importantly, guest materials can work as spacers to be inserted between the MXene nanosheet and prevent the self-stacking of MXene nanosheets. So far, diverse guest materials have been used to hybridize with MXene, including carbon materials (e.g., carbon nanotubes [CNTs],[89–92] graphene,[43,93] N-doped carbon[94,95]), polymers (e.g., poly(vinyl alcohol),[96] pyrrole [PPy],[44,97,98] polyaniline[96]), and metal compounds (e.g., MnO_2,[87,99] $Fe(OH)_3$,[100] MoS_2,[101] SnS_2[102]). Moreover, the mechanical strength of the MXene film can be improved by the hybridization with nanocarbons (reduced graphene oxide [rGO], CNT) through strong π–π stacking interactions or organic polymers by covalent bonding.[85]
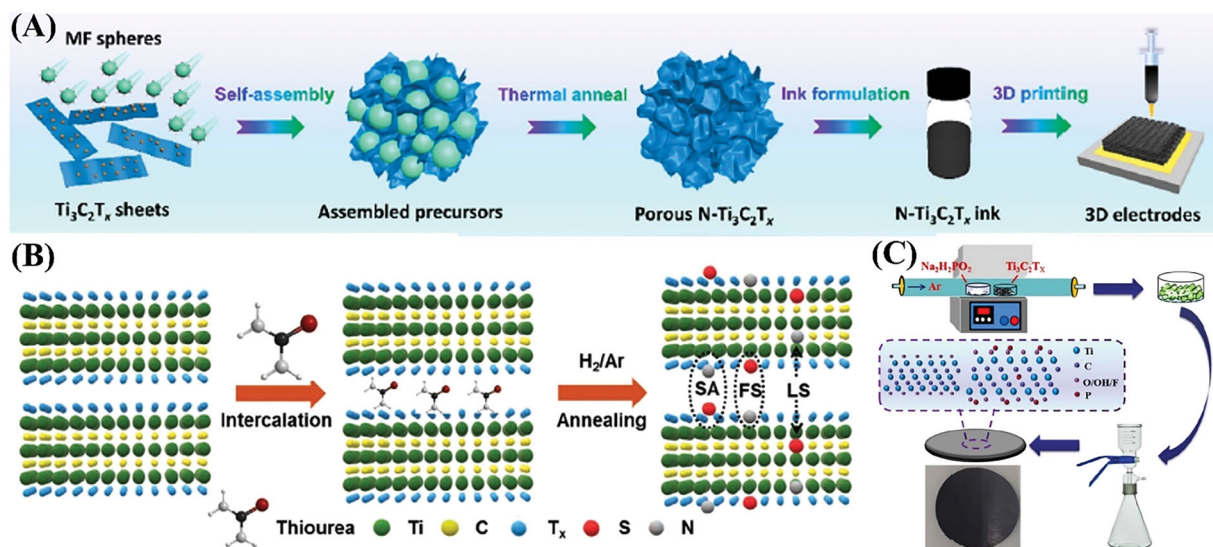
FIGURE 5 (A) Illustration showing the template-assisted synthesis of the freestanding N-Ti$_3$C$_2$T$_x$ electrode using melamine formaldehyde (MF) spheres and 3D printing technology. Reproduced with permission.[82] Copyright 2020, American Chemical Society. (B) Schematic illustration of the synthesis of S, N-codoped MXene. Reproduced with permission.[85] Copyright 2021, Wiley-VCH. (C) Schematic illustration of the preparation of phosphate-doped Ti$_3$C$_2$T$_x$. Reproduced with permission.[84] Copyright 2022, Elsevier.

Carbon materials are promising spacer materials due to their high electronic conductivity and chemical stability. Fan et al.[43] fabricated a Ti$_3$C$_2$T$_x$/holey graphene hybrid film by filtration of the mixture of holey graphene oxide (HGO) and alkalized Ti$_3$C$_2$T$_x$, followed by an annealing treatment (Figure 6A). The charge balance of MXene and HGO colloid was destroyed, and the –F surface groups of MXene were replaced by –OH after adding NaOH. The resultant MXene and HGO agglomerates fasten the vacuum-assisted filtration process. After further annealing, a Ti$_3$C$_2$T$_x$/holey graphene film was obtained. The introduction of holey graphene expanded the interlayer spacing of MXene, which is supported by the (002) diffraction peak shift from 7.2° to 6.3° 2θ, the greatly enlarged specific surface area from 1.5 to 68 m^2 g^{-1}, and formed a highly nanoporous connected network, which is beneficial for the ion and electron transport. Besides, a Ti$_3$C$_2$T$_x$-based hybrid film can be fabricated via electrostatic self-assembly.[91,93] Fu et al.[91] reported a Ti$_3$C$_2$T$_x$/single-walled CNT (SCNT) composite film fabricated by filtrating self-assembled positively charged cetyltrimethylammonium bromide (CTAB)-grafted SCNT and negatively charged Ti$_3$C$_2$T$_x$ colloid. Due to the incorporation of SCNTs, the restacking of MXene was effectively inhibited. The obtained Ti$_3$C$_2$T$_x$/SCNT film showed an enlarged interlayer spacing of 19.77 Å, an expanded c lattice parameter of 39.5 Å and large surface area of 54.5 m^2 g^{-1}.

Polymers possess a high potential as spacers to expand the interlayer spacing of MXene nanosheets due to their favorable electrochemical activity, low cost, and good flexibility. In addition, polymers can be in situ poly-merized on the MXene surface, enabling a good contact with MXenes.[44] Boota et al.[44] prepared well-aligned Ti$_3$C$_2$T$_x$/PPy film with an enlarged interlayer spacing and expanded c lattice parameter (48 Å) by mixing a delaminated Ti$_3$C$_2$T$_x$ suspension and PPy with a subsequent filtration (Figure 6B–E). Because of the Lewis acidic character of Ti$_3$C$_2$T$_x$, it triggered the in situ polymerization of PPy without any additional oxidant agent. The PPy chains not only interacted with the Ti$_3$C$_2$T$_x$ layers, but also aligned between the Ti$_3$C$_2$T$_x$ layers due to the hydrogen bonding between the N–H group of the PPy ring and –O or –F groups on the Ti$_3$C$_2$T$_x$ surface. The expanded interlayer spacing facilitated ion transport, while PPy contributed to the additional pseudocapacitance. Electrochemical poly-merization was used to incorporate PPy into the Ti$_3$C$_2$T$_x$ layers.[103] PPy serving as spacers enlarged the interlayer spacing of Ti$_3$C$_2$T$_x$ from 18.79 to 19.20 Å. Moreover, the strong hydrogen bonding between PPy and the Ti$_3$C$_2$T$_x$ surface not only facilitated the electron and ion transport, but also enhanced the structural stability. Besides, bacterial cellulose (BC) was hybridized with Ti$_3$C$_2$T$_x$ to fabricate a freestanding 3D porous Ti$_3$C$_2$T$_x$ film.[45] In light of the interaction between the O-containing groups of Ti$_3$C$_2$T$_x$ and BC, BC was absorbed with MXene, forming hybrid clusters. After filtration and freeze-drying, a freestanding mixture film was obtained, showing a highly porous structure, enhanced mechanical strength, and fast ionic diffusion pathway (Figure 6F).

Metal compounds (metal oxides, metal sulfides, etc.) are another kind of promising spacer due to their electrochemical activity. For instance, Tian et al.[87] synthesized
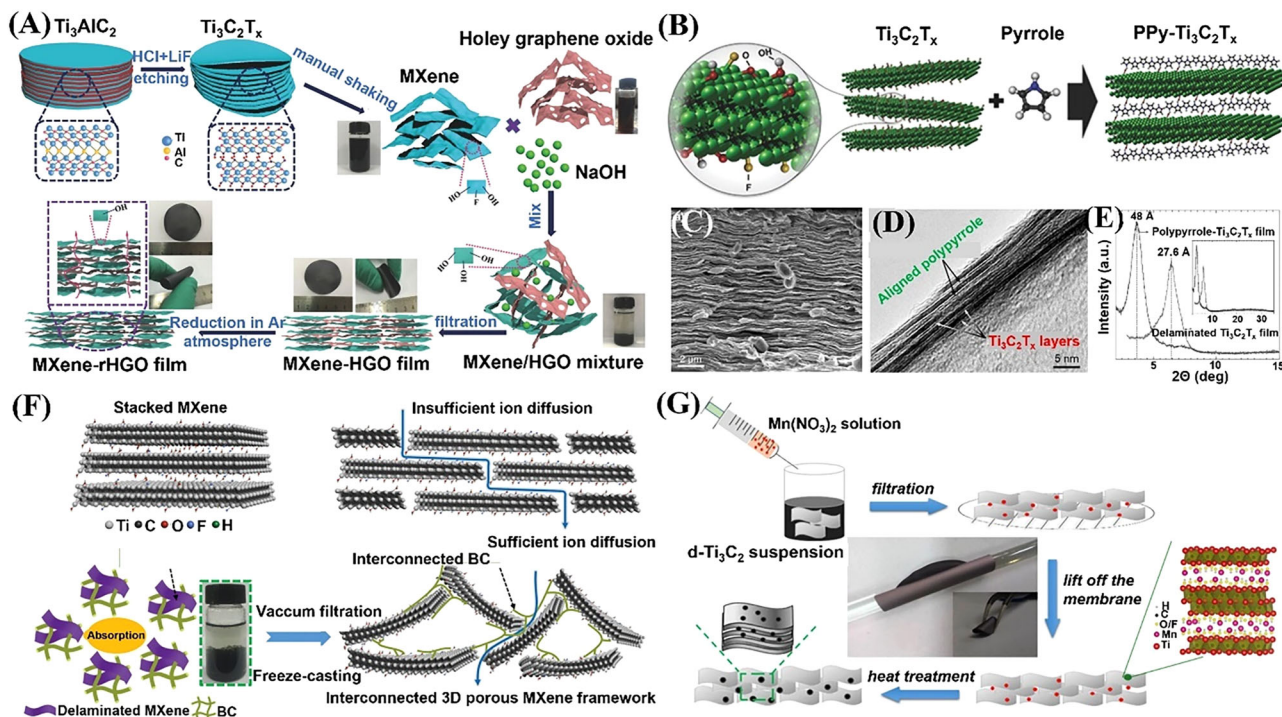
FIGURE 6 (A) Illustration of synthesis of the modified MXene/holey graphene film. Reproduced with permission.[43] Copyright 2018, Wiley-VCH. (B) Schematic illustration of the preparation of PPy-Ti$_3$C$_2$T$_x$. (C) Scanning electron microscopy (SEM), (D) transmission electron microscopy (TEM), and (E) X-ray diffraction (XRD) patterns of PPy-Ti$_3$C$_2$T$_x$. Reproduced with permission.[44] Copyright 2016, Wiley-VCH. (F) Stacked MXene and MXene/bacterial cellulose (BC) composite and corresponding ionic transport pathways. Reproduced with permission.[78] Copyright 2019, Wiley-VCH. (G) Schematic illustration of the synthesis of the free-standing MnO$_x$-Ti$_3$C$_2$ films. Reproduced with permission.[87] Copyright 2019, Wiley-VCH. PPy, pyrrole.

freestanding MnO$_x$–Ti$_3$C$_2$ film by filtrating the mixture of Ti$_3$C$_2$ and Mn(NO$_3$)$_2$, followed by the thermal treatment (Figure 6G). Mn ions were adsorbed by the MXene via the electrostatic interactions, where they transformed in situ to MnO$_x$ after the heating treatment. The presence of MnO$_x$ prevented the MXene layer restacking and increased the layer spacing from 12.14 to 15.23 Å. A summary of the advantages and disadvantages of different MXene structure modification strategies is presented in **Table 2**.

## 2.5 | Fabrication of freestanding MXene-based macroforms

There are diverse approaches for fabricating MXene macroforms (1D fiber/yarn, 2D film, 3D foam) using the MXene solution/ink,[104–107] such as vacuum-assisted filtration,[108] dip coating,[105] self-assembly,[35,109] blade casting,[106] spinning,[34] 3D printing,[107] and rolling.[59] Vacuum-assisted filtration is a widely used technique to prepare films from 2D nanoflakes.[108] Under the vertical downward force induced by the vacuum pump, the MXene flakes are tightly assembled into an inter-

locking layered film on the substrate. The thickness of the film can be controlled by tuning the amount of the MXene flakes. However, this technique is restricted by the time-consumption and energy-consumption process, particularly for thick MXene film. This is because large MXene flakes can quickly cover the pores of the filter membrane, thus hindering the solvent to pass through the filter. Moreover, the slow filtration process would lead to a prolonged contact time between MXene and oxygen, increasing the risk of MXene oxidation. The fast filtration process was realized by using ions to form the MXene microgelation (Figure 7A).[104] The continuous space in the MXene microgel enabled fast water passing, leading to reduced filtration time. Dip coating was also used to integrate MXene nanosheets into various porous templates for fabricating freestanding MXene macroforms (Figure 7B). Zhang et al.[105] prepared a Ti$_3$C$_2$T$_x$/rGO/carbon hybrid foam from graphene oxide (GO), MXene, and melamine foam via dip coating, followed by reduction, freeze-drying, and annealing treatments. The rGO converted from the GO precursor functioned as the conductive binder via the π–π stacking interactions, while the melamine foam template provided a compressible carbon substrate and introduced nitrogen heteroatoms into the Ti$_3$C$_2$T$_x$/rGO

TABLE 2 The structure modification strategies of MXenes for electrochemical energy storage applications.

Strategy	Advantages	Disadvantages	Applications
Ion/polymer intercalation	Creating extra storage space in the interlayer Attracting more ions to be intercalated	Suitable intercalation agents are needed	SCs[75]
Template-assisted porous structure	Forming porous structure Removing template process is needed	Limited effect in shortening the ionic transport paths Low volumetric energy densities	SIBs[24] SCs[76]
Creating pores	Enlarging the accessible surface area Shortening the ionic transport paths	Limited effect in shortening the ionic transport paths	LIBs[80,81] SCs[39]
Vertical alignment	Shortening the ionic transport paths Thickness-independent performance Large volumetric performance metrics	Special surfactants are needed	SCs[38]
Termination group modification	Low content of –F group on the surface Hetero-atom doping can improve the electrochemical performance	Thermal treatment at the high temperature is normally used	LIBs[81] SIBs[82] SCs[84]
Hybridization	Combing the advantage of MXene and other components Expanding the interlayer space	Possibly deteriorating the whole energy densities	SCs[43]

Abbreviations: LIBs, lithium-ion batteries; SCs, supercapacitors; SIBs, sodium-ion batteries.
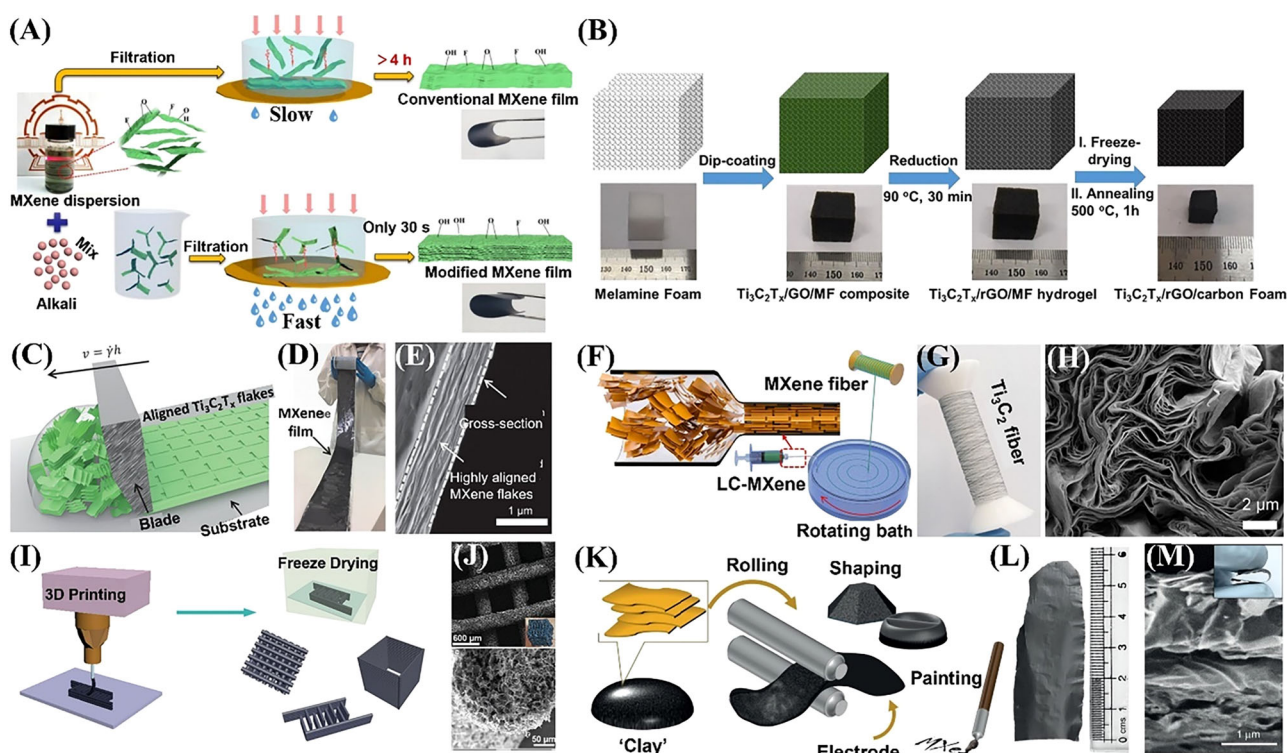
FIGURE 7 (A) Schematic illustration showing the preparation process of the MXene film by vacuum-assisted filtration. Reproduced with permission.[104] Copyright 2021, Engineered Science. (B) Fabrication of the MXene-based hybrid foam. Reproduced with permission.[105] Copyright 2022, Elsevier. (C) Schematic illustration of the blade coating process. (D) Optical image of the MXene-coated Celgard membrane. (E) Scanning electron microscopy (SEM) image of the MXene film fabricated by blade casting. Reproduced with permission.[106] Copyright 2020, Wiley-VCH. (F) Schematic illustration of the wet-spinning setup. (G) Optical image of the $Ti_3C_2T_x$ fiber. (H) Cross-section SEM image of the $Ti_3C_2T_x$ fiber. Reproduced with permission.[34] Copyright 2019, Wiley-VCH. (I) Schematic illustration of the 3D printing and the obtained freestanding 3D architectures. (J) SEM and optical images of freestanding $Ti_3C_2T_x$ microlattice (upper case) and cross-section SEM image of one filament within the microlattice (lower case). Reproduced with permission.[107] Copyright 2020, American Chemical Society. (K) Rolling $Ti_3C_2T_x$ MXene clay to prepare freestanding films. (L) Optical image of a rolled $Ti_3C_2T_x$ MXene film. (M) SEM image of the obtained $Ti_3C_2T_x$ MXene film. Reproduced with permission.[59] Copyright 2014, Springer Nature.

composite. The obtained N-doped hybrid foam shows high compressibility up to 60% (0.25 MPa) and promising electrochemical performance (i.e., 276 F g^{-1} at 0.5 A g^{-1}).

Due to the strong van der Waals forces and hydrogen bonding, MXene nanosheets can be self-assembled into different MXene macroforms (2D films and 3D sponges).[35,110–112] For example, Hu et al.[112] prepared Ti$_3$C$_2$T$_x$ foam by hydrochloric acid induction method to form MXene hydrogel and a subsequent freeze-drying step. Hydrochloric acid was used to decrease the zeta potential of MXene nanosheets, and thus, the repulsion force among the MXene nanosheets was reduced, which further triggered the self-assembly of MXene into the hydrogel. After pre-freezing, the water in the hydrogel was converted into ice. The ice acts as template and would sublimate after freeze-drying, leaving the MXene foam with a cross-linked porous structure. Other methods were also developed to fabricate the self-assembled MXene hydrogels and MXene foams.[113,114] Normally, the obtained foam shows unsatisfactory mechanical properties. Zhao et al.[35] demonstrated an interesting approach to fabricate a flexible Ti$_3$C$_2$T$_x$ film. When the negatively charged Ti$_3$C$_2$T$_x$ the Zn foil, the oxygen-containing terminal groups of Ti$_3$C$_2$T$_x$ were removed, and the electrostatic repulsion interaction among the Ti$_3$C$_2$T$_x$ sheets was weakened. Then, Ti$_3$C$_2$T$_x$ was self-assembled into hydrogel on the Zn foil due to the van der Waals forces and hydrogen bonding. After vacuum drying and freeze-drying, the obtained Ti$_3$C$_2$T$_x$ film with a cross-linked porous network was obtained, exhibiting a high electronic conductivity with a sheet resistance of 8.3 Ω and excellent mechanical properties with a tensile strength of 1.55 MPa and a Young's modulus of 287 MPa.

Blade casting represents a widely used coating technology that allows the continuous and scalable fabrication of films. The highly ordered MXene film was produced by relying on the shear force generated by the doctor blade coating.[106] Zhang et al.[106] fabricated an MXene film with high mechanical strength and electrical conductivity by the blade coating approach (Figure 7C). Due to the high viscosity and good flowability of the high-concentration Ti$_3$C$_2$T$_x$ dispersion (30 mg mL^{-1}), the Ti$_3$C$_2$T$_x$ flakes (an average lateral size of 10 ± 2.1 μm) were aligned under the shear force generated by the transverse motion of the doctor blade. As a result, several meters of MXene film with a thickness of 940 nm was obtained. The film showed a high tensile strength of 568 ± 24 MPa and Young's modulus of 20.6 ± 3.1 GPa, as well as a high electrical conductivity of 15 100 S m^{-1} (Figure 7D,E). Spray coating is another widely used coating technology for scalable film fabrication. Peng et al.[115] demonstrated all-MXene (Ti$_3$C$_2$T$_x$) solid-state interdigital microsupercapacitors via the spray coating of a dTi$_3$C$_2$T$_x$ solution and a photoresist-free direct laser cutting approach. Large-size Ti$_3$C$_2$T$_x$ flakes with a lateral size of 3–6 μm were first deposited on a glass substrate as the current collector, and then the small-size Ti$_3$C$_2$T$_x$ flakes ($\sim$1 μm) with rich defects and edges were deposited, serving as an electroactive layer.

The wet-spinning technique was adopted to fabricate MXene fibers using the aqueous ink containing highly ordered liquid-crystalline MXene flakes.[34] Zhang et al.[34] found that small MXene flakes showed a high critical isotropic-nematic phase transition concentration, while large MXene flakes exhibited a low critical transition concentration. The nematic liquid crystalline phase with long-range orientational ordering was conducive for fabricating MXene fibers by the wet-spinning method (Figure 7F–H). The effect of the MXene flake size, coagulation bath composition, and nozzle size on the fiber properties was systematically investigated. Remarkably, wet-spun Ti$_3$C$_2$ fibers with a diameter of 34.5 μm displayed a high electric conductivity of $\sim$7750 S cm^{-1}.

In addition, 3D printing has been applied to prepare 3D MXene architectures.[107] Yang et al.[107] fabricated a freestanding MXene architecture with a high surface area via an extrusion-based 3D printing approach. The aqueous Ti$_3$C$_2$T$_x$ ink containing MXene with a thickness of 1–3 nm and lateral size of 8 μm was used. Different wet freestanding Ti$_3$C$_2$T$_x$ architectures, such as 3D woodpiles, hollow rectangular prisms, and interdigitated electrode configurations, were directly printed in the air, and their shapes could be well maintained after the printing process (Figure 7I). After freeze-drying, the Ti$_3$C2T$_x$ 3D architectures were retained relying on the internal integrity and the low shrinkage of external structure. The obtained Ti$_3$C$_2$T$_x$ architectures with a microlattice structure showed individually printed filaments with a diameter of 326 ± 13 μm and porous interconnected networks (Figure 7J). Rolling was also used to prepare the Ti$_3$C$_2$T$_x$ films from Ti$_3$C$_2$T$_x$ "clay."[59] Ghidiu et al.[59] etched Ti$_3$AlC$_2$ with the LiF-added HCl solution, followed by heating and washing. The obtained sediment appearing as a clay-like paste was rolled into a film (Figure 7K,M). The dried film showed high flexibility and an overall shearing of the multilayer particle morphology from cross-section (Figure 7M). The advantages and disadvantages of different fabrication methods for freestanding MXene macroforms are listed in **Table 3**. It is important to further develop a suitable approach for the scalable manufacture of freestanding MXene macroforms.

3 | MXENE-BASED MACROFORMS FOR ELECTROCHEMICAL ENERGY STORAGE

Owing to their ability to store intermittent energies and continuously release energy, electrochemical energy

TABLE 3 Advantages and disadvantages of different fabrication methods for freestanding MXene macroforms.

Methods	Advantages	Disadvantages	Applications
Vacuum-assisted filtration	Simple, thickness controllable	Size is limited by the instrument Time consuming	NIBs[24] SCs[108]
Dip coating	Simple and scalable	Freestanding substrates are required Week adhesion to the substrate	SCs[105]
Self-assembly	Mesoporous structure	Introducing other components Freeze-drying technique is required Limited size	SCs[35,109]
Coating	Simple and scalable	Random layers stacking High-quality solution required	SCs[115]
Spinning	Simple and scalable	Time consuming High cost of equipment	SCs[34]
3D printing	Controllable architectural, simple and scalable	High cost of equipment	SCs[107]
Rolling	Simple and scalable	Large flakes are required	SCs[59]

Abbreviation: SCs, supercapacitors.

storage systems (e.g., batteries, supercapacitors) have been increasingly investigated recently and they have demonstrated successful applications in portable electronics and electric vehicles.[116] MXenes as electrode materials have been widely used in batteries and supercapacitors, because of their high electronic conductivity, abundant surface groups, and wide chemical and structural variety.[72] Besides, the freestanding MXene-based macroforms can be easily fabricated from MXene solutions and can be directly used as electrodes.

3.1 | MXene-based macroforms for batteries

3.1.1 | MXene macroforms as electrode materials in batteries

Theoretically, MXenes possess a low energy barrier for metal-ion diffusion, which can be beneficial for achieving high-rate performance.[117–120] Er et al.[119] simulated the adsorption of different metal ions (Li$^+$, Na$^+$, K$^+$, and Ca^{2+}) on Ti$_3$C$_2$ with DFT calculations. The calculated diffusion barriers for Li$^+$, Na$^+$, K$^+$, and Ca^{2+} are 0.068, 0.096, 0.103, and 0.118 eV, respectively. Meanwhile, the predicted capacities of Ti$_3$C$_2$ for Li$^+$, Na$^+$, K$^+$, and Ca^{2+} ion storage were 447.8, 351.8, 191.8, and 319.8 mAh g^{-1}, respectively. Similarly, Fan et al.[120] investigated the V$_3$C$_2$ monolayers as anode materials for metal-ion (Li$^+$, Na$^+$, K$^+$, and Ca^{2+}) batteries by DFT calculations. They disclosed that the V$_3$C$_2$ MXene showed a low diffusion barrier for Li$^+$ (0.04 eV), Na$^+$ (0.02 eV), K$^+$ (0.01 eV), and Ca^{2+} (0.04 eV), demonstrating that the V$_3$C$_2$ monolayer has the potential to be a high-rate capable anode material. However, the real appli-

cation of MXenes is limited by their self-stacking, which leads to a limited interlayer spacing and accessible surface area. Hence, various strategies (intercalation, surface functional group modification, hybridization, etc.) were developed to prevent the re-stacking issue of MXenes and optimize their electrochemical performance.

Intercalating ions (Na$^+$, Zn^{2+}, Al^{3+}, Sn^{4+}, etc.) or small molecules into the MXene interlayer space has been employed to expand the interlayer gap of MXene and enhance their ionic migration kinetics.[121,122] For instance, Lu et al.[122] synthesized the Al^{3+}-intercalated Ti$_3$C$_2$T$_x$ MXene film as anode for LIBs. Benefiting from the Al^{3+} intercalation, the expanded interlayer space of MXenes facilitated the Li$^+$ ion transfer. In addition, more positive charge on the Ti surface has been found compared to that of pristine MXenes due to the loss of local electrons. The stronger Coulomb force induced by the introduction of Al^{3+} also contributed to a larger interlayer spacing. Impressively, a high specific capacity of 152 mAh g^{-1} after 10 cycles and the capacity retention of 89.7% after 100 cycles at 320 mA g^{-1} were achieved for Al^{3+}-intercalated Ti$_3$C$_2$T$_x$ film in LIBs. Besides, Xu et al.[123] reported a freestanding Ti$_3$C$_2$T$_x$/CTAB paper via the filtration method, in which CTA$^+$ ions as the intercalation agent were introduced into Ti$_3$C$_2$T$_x$. The MXene paper with an enlarged interlayer spacing of 15.2 Å enabled enhanced diffusion kinetics of Mg^{2+}. Simultaneously, the nudged elastic band calculation verified that the diffusion barrier of Mg^{2+} on the CTA$^+$-intercalated Ti$_3$C$_2$T$_x$ surface is lower than that of the pristine Ti$_3$C$_2$T$_x$ surface. As a result, the fabricated paper electrode exhibited a large volumetric specific capacity of 300 mAh cm^{-3} at 50 mA g^{-1} for Mg-ion batteries. Moreover, the superior cycling performance with a capacity of 135 mAh cm^{-3} at 0.2 A g^{-1} for 250 cycles with nearly 100%

Coulombic efficiency was achieved. In addition, Mashtalir et al.[74] used DMSO and urea as the intercalants to prepare delaminated Ti_3C_2 with an expanded c-lattice parameter from 19.5 to 35 Å and 25 Å, respectively. A freestanding binder-free MXene paper was made through simple filtration, exhibiting much better Li^+ storage capability (410 mAh g^{-1}) than non-delaminated Ti_3C_2 (~100 mAh g^{-1}) after 100 cycles at 1°C.

The highly porous structures of MXene-based macroforms provide the maximum number of exposed surface sites, which is thus beneficial for high-rate charge transfer. A 3D porous MXene structure was easily constructed through a polymethyl methacrylate (PMMA)-template method.[79] PMMA spheres enabled MXene sheets to stack into a 3D structure with abundant macropores. The as-obtained 3D interlinked structure composed of massive pores enhanced electrolyte ion accessibility and electron transfer, as well as the structural stability. The demonstrated method was also applicable to fabricate microporous film of other MXenes (e.g., Mo_2CT_x, V_2CT_x). Remarkably, reversible capacities of about 295, 290, and 310 mAh g^{-1} were retained for 3D $Ti_3C_2T_x$, Mo_2CT_x, and V_2CT_x films, respectively, after 1000 cycles at a high rate of 2.5 C in SIBs. Likely, sulfur was used as a bifunctional template to form a microporous structure and tune the surface chemistry of MXenes.[124] The obtained freestanding S-doped mesoporous $Ti_3C_2T_x$ film was directly used as an anode for SIBs, delivering a high-volumetric capacity of 625.6 mAh cm^{-3} at 0.1 A g^{-1} and a long-term cycling stability over 5000 cycles.

Surface engineering of MXenes is an effective strategy to modify the intrinsic electronic structure, adjust the interlayer spacing, and enhance the redox reactivity.[125] The ion storage capacities strongly depend on the properties of the surface functional groups, which have been intensively verified by DFT calculations and experiments. For instance, Li et al.[126] synthesized Ti_3C_2 MXene with diverse halogen terminals (e.g., –Cl, –Br, –I, –BrI, and –ClBrI) through a Lewis acidic melt etching route to investigate the relation between the surface terminal and MXene properties. They revealed that MXenes containing –Br and –I showed a reversible reaction, resulting in an extraordinary electrochemical performance (i.e., 97.6 and 135 mAh g^{-1} at 0.5 A g^{-1}, respectively) in aqueous ZIBs. By contrast, no reversible conversion reactions were detected for the –O, –F, and –Cl terminals on the MXene. Recently, our group reported a freestanding Nb_4C_3 film with redox-active phosphorus−oxygen (–PO_2) terminals by annealing the hybrid membrane consisting of $Nb_4C_3T_x$ MXene and black phosphorus (Figure 8A,B).[24] The obtained PO_2-terminated Nb_4C_3 showed greatly enhanced carrier density (by fourfold), improved electronic conductivity (by 12.3-fold at 300 K), and extra redox active sites compared

with the O-terminated counterpart. In addition, the PO_2 terminals could release the induced stress during Na^+ insertion/extraction. Importantly, a high specific capacity of 221 mAh g^{-1} at 0.05 A g^{-1} and excellent cycling stability over 2000 cycles at 1 A g^{-1} were achieved for the PO_2-terminated Nb_4C_3 in SIBs (Figure 8C).

Materials with different dimensions (e.g., 0D nanoparticles, 1D nanotubes, and 2D nanosheets) were hybridized with 2D MXene nanosheets to build hierarchical architectures with enhanced electron/ion transport and stabilized the structural integrity. MXenes with a highly conductive network and excellent mechanical properties can guarantee fast electron transfer and also accommodate the volume variation of the guest material. In turn, the guest materials can function as spacers to prevent the stacking of MXene layers. Moreover, redox-active guest materials contribute to additional capacity. Redox-active nanoparticles (e.g., Si, MnO_2, etc.) have been widely used to hybridize with MXene.[117,127] For example, Si nanoparticles were uniformly loaded onto the $Ti_3C_2T_x$ nanosheets by vacuum filtration, and the Si/MXene composite papers exhibited high structural stability and flexibility.[127] When applied as the anode in LIBs, the freestanding Si/MXene paper showed superior electrochemical performance with a high specific capacity of 2118 mAh g^{-1} at 200 mA g^{-1} and the steady cycling ability over 200 cycles with a high maintained specific capacity of 1672 mAh g^{-1} at 1 A g^{-1}. Besides, manganese oxide (MnO_x) nanoparticles were evenly anchored between accordion-like $Ti_3C_2T_x$ layers for improving zinc-ion storage (Figure 8D).[117] $MnO_x@Ti_3C_2T_x$ electrode with a hierarchically layered structure endows the parallel circuitry; thus, the rapid transport pathways for electrons and ions were constructed. Consequently, the electrode depicted the high-rate capability with a high specific capacity of 44 mAh g^{-1} even at a high current density of 10 A g^{-1} (Figure 8E,F).

One-dimensional CNTs have also been used to hybridize with various MXenes (Ti_3C_2, Ti_2C, V_2C, and Nb_2C). CNTs between the MXene layers can bridge the interlayer gaps, ensuring an isotopically high electrical conductivity and improving their mechanical properties. For example, Xie et al.[89] reported the porous Ti_3C_2 MXene/CNT composite electrodes for Na^+-based energy storage devices. The Ti_3C_2/CNT hybrid was self-assembled by the electrostatic attraction between negatively charged MXene nanosheets and positively charged CNTs. CNTs worked as the space filler efficiently protecting the delaminate structure of MXene by forming a well-defined porous structure. Such a unique structure benefited the electrolyte transport and ion access to the electrode. Consequently, an excellent rate performance (i.e., 89 mAh cm^{-3} at 5 A g^{-1}) and cycling stability with a capacity of 345 mAh cm^{-3} over 500 cycles at 100 mA g^{-1} were obtained.
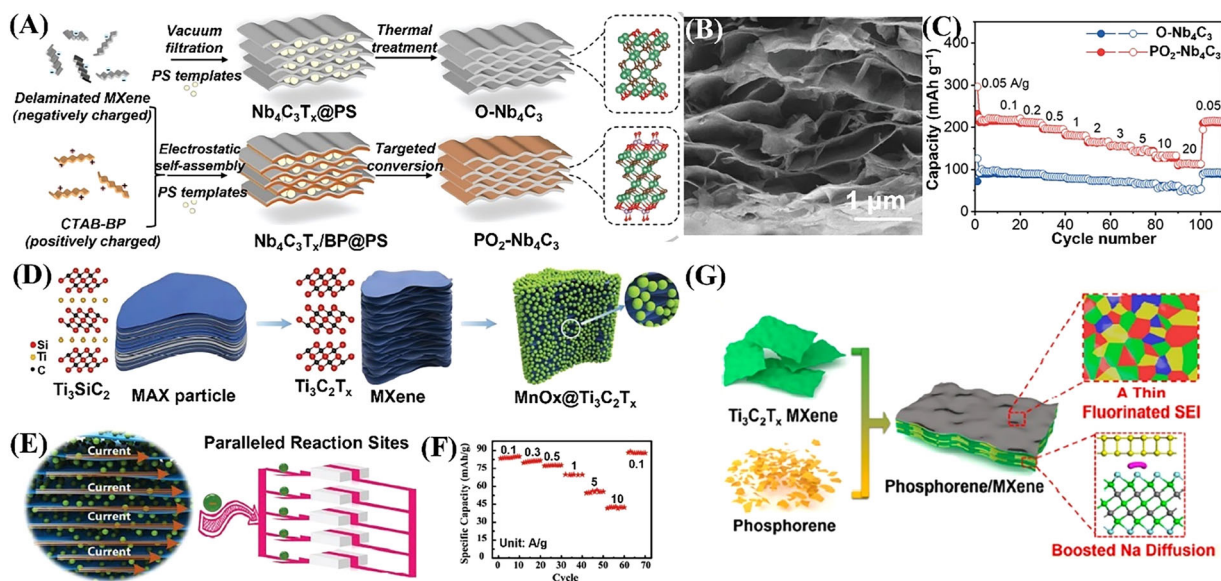
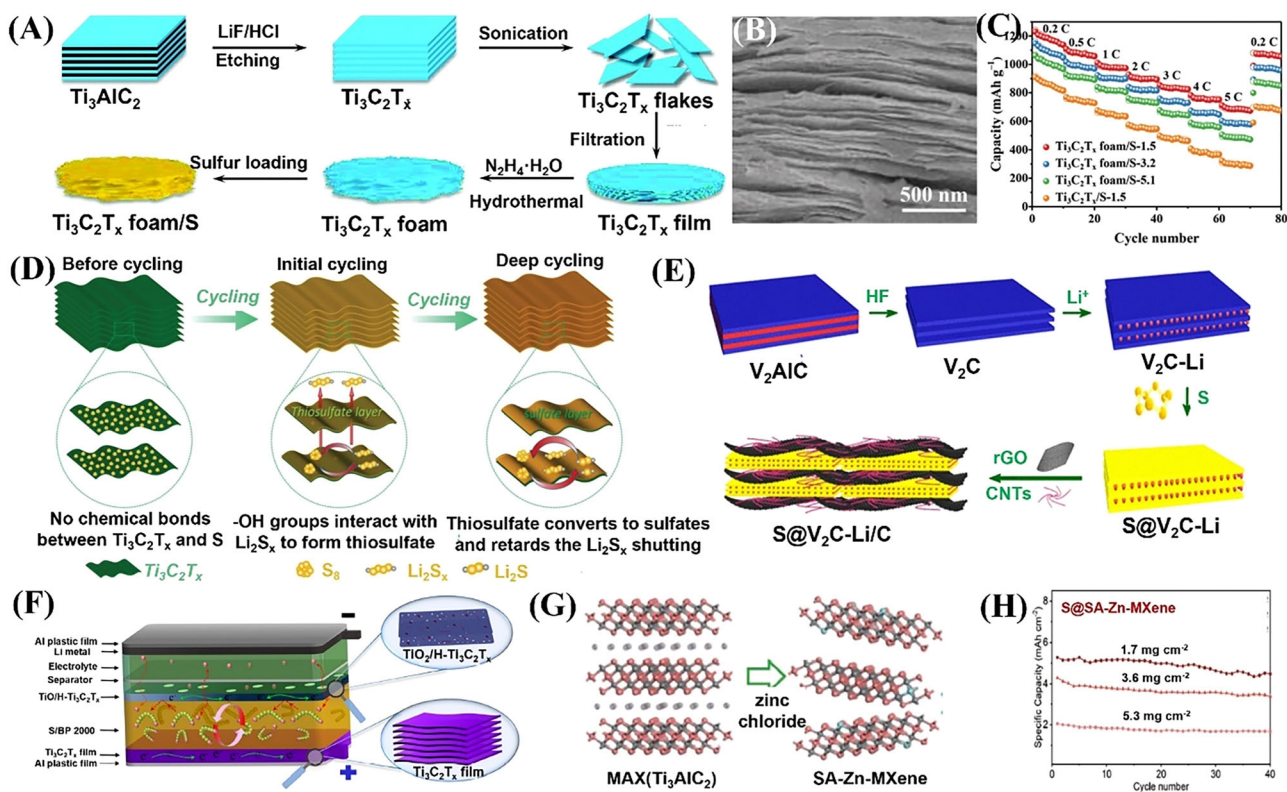**FIGURE 8** (A) Schematic illustration showing the synthesis of the freestanding PO_2–Nb_4C_3 and O–Nb_4C_3 films. (B) Scanning electron microscopy (SEM) image of the PO_2–Nb_4C_3 film. (C) The performance comparison of the PO_2–Nb_4C_3 and O–Nb_4C_3 anodes in sodium-ion batteries (SIBs) at 0.05 A g^{-1}. Reproduced with permission.[24] Copyright 2022, Wiley-VCH. (D) Schematic illustration showing the fabrication of MnO_x@$Ti_3C_2T_x$. (E) Schematic illustration showing the parallel circuitry at the nanoscale of MnO_x@$Ti_3C_2T_x$ and (F) the corresponding rate performance in zinc-ion batteries (ZIBs). Reproduced with permission.[117] Copyright 2019, Wiley-VCH. (G) Schematic illustration showing the synthetic processes of the phosphorene/MXene hybrid structure and the demonstration of positive effects as anode materials in SIBs. Reproduced with permission.[118] Copyright 2020, American Chemical Society.

Two-dimensional materials (e.g., graphene, MoS_2, phosphorene, etc.) are prone to be face-to-face loaded on MXene, forming horizontally alternating layers of 2D structures. Freestanding MXene-based/2D heterostructures with high tap densities can thus be easily fabricated. For instance, a phosphorene/MXene 2D composite was produced by a vacuum freeze-drying process of a colloidal mixture of few-layer phosphorene and $Ti_3C_2T_x$ MXene nanoflakes (Figure 8G).[118] The structural expansion of the electrochemically active phosphorene nanosheets was efficiently alleviated, and the migration of both electrons and sodium ions was also significantly improved. Moreover, DFT calculations verified the enhancement of Na$^+$ affinities and diffusion kinetics in the phosphorene/MXene heterostructure. Impressively, the hybrid electrode achieved a high reversible specific capacity of 535 mAh g^{-1} at 0.1 A g^{-1} and superior cycling stability with a high capacity retention of 87% after 1000 cycles at 1 A g^{-1}. Recently, Ma et al.[128] constructed an MXene/rGO hybrid film with a 3D porous structure using a simple electrolyte-induced self-assembly approach. With the assistance of the GO skeleton, MXene can be transformed into a dense and stacked 3D porous architecture. When used as an anode of LIBs, the as-fabricated freestanding electrode exhibited a high specific capacity of 335.5 mAh g^{-1} at 0.05 A g^{-1} and excellent cycling stability without capacity decay after 1000 cycles at 1 A g^{-1}.

3.1.2 | MXene macroforms as sulfur hosts in Li–S batteries

Lithium–sulfur batteries (LiSBs) have been seen as one of the more promising candidates for next-generation energy storage devices by virtue of their high energy density (2600 Wh kg^{-1}) and low cost.[129–134] Nevertheless, the practical application of LiSBs still suffers from the fast capacity fading and low Coulombic efficiency, owing to the problematic issues of the sulfur cathode: (1) the shuttle effect of lithium polysulfides (LiPSs) (Li_2S_n, $4 \leq n \leq 8$) between the anode and cathode and (2) sluggish redox reaction kinetics. A general strategy to tackle these challenges is physically and chemically entrapping LiPSs with non-polar host materials.[135] Among varying host materials, 2D MXenes stand out as a great choice for LiSBs because of their excellent electronic conductivity, tunable functional groups, and high mechanical strength. Long-chain polysulfides, such as Li_2S_4, Li_2S_6, and Li_2S_8, can be effectively captured by forming Ti–S, H–S, and Li–O bonds with $Ti_3C_2T_x$ MXene based on the Lewis acid–base interactions and the Coulombic interactions with $Ti_3C_2T_x$ MXene. In addition, short-chain sulfides (Li_2S and Li_2S_2) can be entrapped by the –O termination on the MXene.[136,137]

The fabricated MXene-based macroforms with robust mechanical strength and high electronic conductivity were demonstrated as promising materials to host high-loading

FIGURE 9 (A) Schematic illustration showing the synthesis of the self-supporting $Ti_3C_2T_x$ foam/S cathode. (B) Cross-sectional scanning electron microscopy (SEM) image of $Ti_3C_2T_x$ film. (C) Rate performance of $T_3C_2T_x$ foam/S. Reproduced with permission.[129] Copyright 2018, Royal Society of Chemistry. (D) Mechanism of confining polysulfides in the $Ti_3C_2T_x$ by an in situ grown sulfate complex protective layer. Reproduced with permission.[29] Copyright 2019, Wiley-VCH. (E) Fabrication of the free-standing $S@V_2C$–Li/C electrode. Reproduced with permission.[130] Copyright 2020, Royal Society of Chemistry. (F) Configuration of the flexible Li–S battery based on MXene-based sandwich cathode. Reproduced with permission.[131] Copyright 2022, American Chemical Society. (G) Fabrication of SA-Zn-MXene via etching with molten zinc chloride. (H) Cycling performances of S@SA-Zn-MXene (DIB) with different sulfur loadings at 0.2 C. Reproduced with permission.[132] Copyright 2020, Wiley-VCH. SA, surface absorption.

sulfur for practical LiSB applications. For instance, Zhao et al.[129] designed a self-supporting $Ti_3C_2T_x$ foam via filtration of single-layer $Ti_3C_2T_x$ flake solution and subsequent hydrothermal treatment of $Ti_3C_2T_x$ film. Afterward, sulfur was impregnated into the $Ti_3C_2T_x$ foam and $Ti_3C_2T_x$ foam/S cathodes were obtained (Figure 9A,B). The $Ti_3C_2T_x$ foam showed physical and chemical co-adsorption of polysulfides, which was enabled by a well-defined porous structure with abundant exposed Lewis acidic sites. Remarkably, the $Ti_3C_2T_x$ foam/S cathode with a high sulfur loading of 5.1 mg cm^{-2} displayed a high initial specific capacity of 1226.4 mAh g^{-1} at 0.2 C, outstanding rate capability (i.e., 711.0 mAh g^{-1} at 5 C), and a magnificently long lifetime over 1000 cycles with the capacity retention of 75% (Figure 9C). As the MXene foam substituted the conventional high-weight metal current collectors, maximization of gravimetric energy density to 1297.8 W h kg^{-1} was demonstrated for LiSBs. Besides, a robust and freestanding $Ti_3C_2T_x$/S conductive paper cathode was developed by Zhang et al.[29] In the cathode, $Ti_3C_2T_x$ nanosheets were

tightly compacted and woven into an interconnected network. Due to the reaction between polysulfides and −OH on the surface of $Ti_3C_2T_x$, a thiosulfate layer was generated and further converted to a sulfate complex during the initial cycling (Figure 9D). The in situ formed sulfate complex layer as a protective film effectively inhibited the shuttle effect of LiPSs, endowing the $Ti_3C_2T_x$/S paper with a high specific capacity of 1383 mAh g^{-1} at 0.1 C, excellent rate performance (i.e., 1075 mAh g^{-1} at 2 C), and ultra-low capacity decay of 0.014% per cycle after 1500 cycles at 1 C. In addition, Chen et al.[130] prepared freestanding S@Li$^+$-intercalated V_2C MXene/rGO-CNT (denoted S@V_2C-Li/C) for LiSBs (Figure 9E). rGO and CNTs provided a robust and conductive backbone, while Li-intercalated V_2C enabled improved chemical absorption of polysulfides and lithium-ion transport kinetics owing to its high polarity and expanded interlayer distance. As a result, the electrode exhibited an initial specific capacity of 1140 and 1030 mAh g^{-1} after 100 cycles at 0.1 C, as well as long-term cycling stability over 500

cycles at 2 C with a capacity decay rate of 0.051% per cycle.

After oxidation of MXene, the atoms on the MXene surface can convert to functional sites with high efficiency in trapping polysulfides and catalyzing their conversion. For example, by controlled oxidation of few-layer MXenes, an MXene-based freestanding and sandwich-like composite material was prepared. Such a material consisted of freestanding $Ti_3C_2T_x$ films, sulfur, and TiO_2 nanorods anchored porous $Ti_3C_2T_x$ (TiO_2/H-$Ti_3C_2T_x$) layers, and it was used as the cathode for LiSBs (Figure 9F).[131] TiO_2 nanorods were in situ transformed from $Ti_3C_2T_x$, while the termination of $Ti_3C_2T_x$ was oxidized to –O, showing a catalytic effect in accelerating conversion kinetics among LiPSs and Li_2S. DFT calculations demonstrated that on the (110) surface of TiO_2, Ti–S and Li–O bonds could be easily formed because of the strong electrostatic interaction between Ti/O atoms in TiO_2 and S/Li atoms in Li_2S_n. Thus, there is a strong sulfur anchoring effect was induced by TiO_2. In terms of the reaction kinetics, $Ti_3C_2T_x$ with high content of –O showed low Li_2S and Li_2S_6 decomposition barriers, and a low Li^+ diffusion energy barrier, enabling an efficient catalytic effect for the reverse reaction between Li_2S and S_8. Consequently, the obtained sandwich electrode demonstrated a high-rate capability (i.e., 740 mAh g^{-1} at 2 C) and long cycling stability over 500 cycles at 1 C with high capacity retention of 81%. Using CO_2 as the oxidation agent, Lee et al.[138] obtained CO_2-oxidized delaminated $Ti_3C_2T_x$-MXene (Oxi-d-$Ti_3C_2T_x$) freestanding sheets. When Oxi-d-MXenes were used as both the sulfur host and coating layer on separators, the assembled LiSBs showed a high Coulombic efficiency of nearly 99% and maintained a capacity of about 900 mAh g^{-1} after 300 cycles at 1 C.

In addition, loading single-atom catalysts (e.g., Pt, Co, Fe, Ni, etc.) on MXene can maximize the catalytic effect and promote the conversion of LiPSs.[132] Single-atom Zn-implanted Ti_3C_2 MXene (denoted SA-Zn-MXene) was fabricated as the sulfur host by etching the Al layer of Ti_3AlC_2 in molten $ZnCl_2$ (Figure 9G).[132] The high electronegativity enabled the atomic Zn in MXene to show a strong interaction with polysulfides, boosting the sulfur species conversion kinetics. It was also revealed that the nucleation of Li_2S_2/Li_2S on the MXene layer was accelerated by the uniformly dispersed Zn atoms during the redox reaction. As a result, the SA-Zn-MXene/S freestanding cathode delivered a high capacity of 1136 mAh g^{-1} at 0.2 C, high-rate capability (i.e., 640 mAh g^{-1} at 6 C), and long-term cycling stability over 200 cycles at 4 C with the capacity retention of 80%. Besides, a remarkable areal capacity of 5.3 mAh cm^{-2} was achieved by the SA-Zn-MXene/S cathode, when the sulfur loading reached 5.3 mg cm^{-2} (Figure 9H).

3.1.3 | MXene macroforms as the metal host in metal batteries

Rechargeable metal batteries are promising alternatives for next-generation high-energy-battery devices, owing to the high theoretical capacity and low electrochemical potential of the metal anodes.[139–143] Electrochemically active metal anodes, such as Li, Na, K, Zn, Mg, and Ca, present plating/stripping mechanisms on the anode side of metal batteries. The nucleation process of metal ions during the initial plating plays a vital role in determining the continuous metal plating/stripping.[144,145] According to the tip-growth mechanism, the metal edges and tips with a high curvature show a higher electric field and thus attract rich metal ions to nucleate. This behavior leads to the metal dendrite formation after repeated charge/discharge cycles, resulting in a short circuit or safety issues for the battery device. In addition, due to their host-free nature, metal anodes suffer large volume changes during the plating/stripping process, which worsens the interfacial ionic transport.[146]

To suppress the above-mentioned issues associated with the metal anodes, a variety of strategies have been developed. For instance, the strategy of employing 3D hosts with metal-philic functional groups to homogenize the electric field and ion flux hereby guide uniform nucleation and deposition of metal ions was developed. Moreover, 3D hosts can accommodate the volume change of metal and reduce the local current density to delay the dendrite formation based on the "Sand's time" model.[147] Due to the outstanding electronic conductivity, abundant functional groups (e.g., –OH, –Cl, –F, and –O), easily tailored structure, and high mechanical strength, MXene-based macroforms are validated theoretically and experimentally as promising metal hosts. Ha et al.[148] studied the Li metal nucleation and growth behavior on the $Ti_3C_2T_x$ with a large number of oxygen and fluorine functional groups. They disclosed that the fluorine terminals contributed to the formation of the homogeneous and durable solid–electrolyte interphase (SEI) layer mainly consisting of LiF, while the oxygen terminals reduced the Li nucleation energy barrier due to a high Li adsorption energy. Therefore, Li atoms penetrated the SEI layer and underwent homogeneous nucleation on the highly lithophilic $Ti_3C_2T_x$ surface. In particular, uniformly dispersed Li nanoparticles with a diameter of 10–20 nm would evolve into close-packed nanoclusters, further forming a dense Li metal layer. The unique MXene substrate enabled the stable Li deposition with a high Coulombic efficiency of >99.0% over 1000 cycles at 0.5 mA cm^{-2} with a capacity of 1 mAh cm^{-2}. Besides, Tian et al.[139] synthesized a freestanding $Ti_3C_2T_x$ MXene@Zn paper by electroplating Zn on the $Ti_3C_2T_x$ paper in 2 M $ZnSO_4$ electrolyte
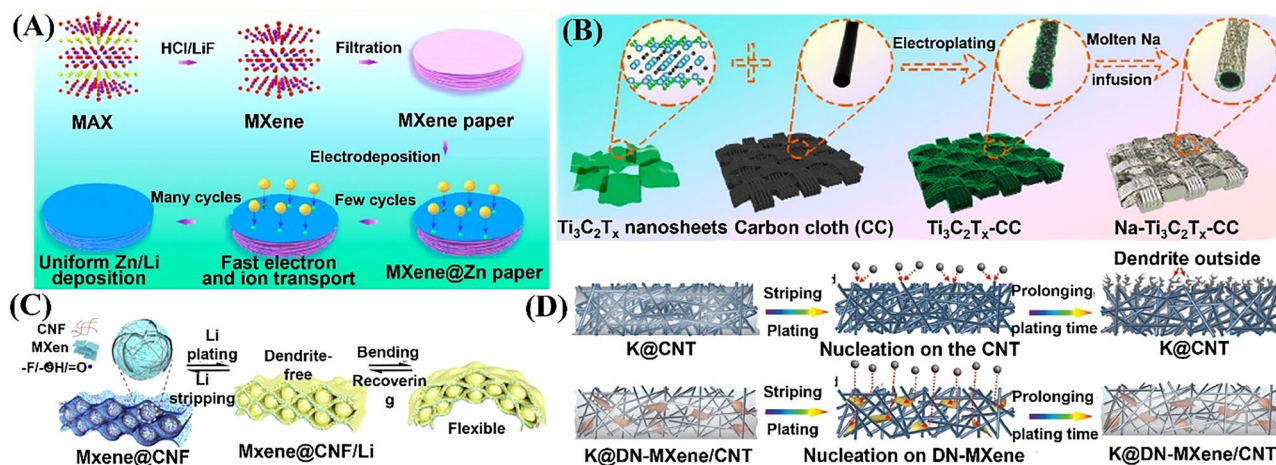
FIGURE 10 (A) Schematic diagram showing the fabrication of the $Ti_3C_2T_x$ MXene@Zn paper and its morphology evolution during the Zn/Li stripping/plating process. Reproduced with permission.[139] Copyright 2019, American Chemical Society. (B) Fabrication process of the $Ti_3C_2T_x$–CC skeleton and the Na–$Ti_3C_2T_x$–CC anode. Reproduced with permission.[140] Copyright 2020, American Chemical Society. (C) Schematic diagram of the Li plating/stripping on MXene@CNF film. Reproduced with permission.[141] Copyright 2020, Elsevier. (D) Schematic illustration showing the preparation of the freestanding DN-MXene/CNT and K@DN-MXene/CNT anodes. Reproduced with permission.[142] Copyright 2020, Wiley-VCH. CC, carbon cloth; CNF, cellulose nanofiber; CNT, carbon nanotube.

(Figure 10A). The $Ti_3C_2T_x$/Zn paper exhibited superior Zn plating/stripping cycling stability for 400 cycles (over 300 h) with an average Coulombic efficiency of 94.13% at 1 mA cm^{-2} and 1 mAh cm^{-2} in a symmetric cell. The enhanced cycling stability was ascribed to the desired merits of the MXene films, such as high conductivity, excellent hydrophilicity for fast ion transport, and a high specific surface area to accommodate Zn deposition. Moreover, Zn in the $Ti_3C_2T_x$/Zn paper served as a high-affinity alloy agent to promote the Li nucleation and growth and thus producing the dendrite-free Li metal anode. Recently, Fang et al.[140] prepared an MXene ($Ti_3C_2T_x$)-coated carbon cloth ($Ti_3C_2T_x$-CC) by a constant-voltage electrophoretic deposition process in the $Ti_3C_2T_x$ dispersion (Figure 10B). Benefiting from the high Na affinity of –F and –O surface groups of $Ti_3C_2T_x$ MXene, the wettability of carbon cloth toward molten Na was apparently improved, and Na–$Ti_3C_2T_x$–CC composite was obtained by thermal infusion of molten Na. The tenacious carbon cloth ensured a robust and highly conductive metallic network, while sodiophilic $Ti_3C_2T_x$ effectively decreased the local current density and guided the even sodium deposition along the MXene architecture, resulting in a transverse smooth "sheet-like" sodium deposition surface. As a result, the Na–$Ti_3C_2T_x$–CC anode showed a long cycling life of 300 h at 5 mA cm^{-2} with a capacity of 1 mAh cm^{-2}. To prevent the restacking of MXene nanosheets and improve the mechanical strength of the MXene films, cellulose nanofibers were hybridized with MXene nanosheets, and a flexible $Ti_3C_2T_x$ MXene/cellulose nanofiber (MXene@CNF) film was fabricated by the facile spin steaming method

(Figure 10C).[141] MXene@CNF film with the interlocked structure demonstrated high mechanical strength and stability. Ti_3C_2 with –F terminals showed higher binding energy toward Li (−2.70 eV) than Ti_3C_2 MXene (−2.47 eV), which can work as a nucleation substrate to guide uniform Li$^+$ nucleation and dendrite-free growth. Consequently, the ultrathin MXene@CNF/Li composite anodes (25 μm thick) showed stable Coulombic efficiency for 250 cycles at 1 mA cm^{-2} and high stability for over 1300 h at 0.5 mA cm^{-2}.

Regulation of MXenes or hybridizing MXenes with nucleating agents to enhance the metal-philic property has been demonstrated to be the vital method to guide the uniform nucleation and growth of metal anodes. For example, a titanium-deficient Ti_3CN-MXene/CNT (as DN-MXene) film was designed as the potassium metal host (Figure 10D).[142] The freestanding and highly conductive scaffold reduced the local current density and homogenized the ionic flux, while the highly potassiophilic DN-MXene film induced uniform potassium nucleation on the scaffold. Consequently, the K@DN-MXene/CNT anode showed stable high Coulombic efficiencies of 98.6% over 200 cycles with a dendrite-free feature and a long cycle life for 300 h at 0.5 mA cm^{-2} with a low overpotential of 0.3 V. Besides, a hybrid $Na_3Ti_5O_{12}/Ti_3C_2$ nanoarchitecture with CTAB stabilization was fabricated and used as the matrix for the Na metal anode from CTAB-pretreated Ti_3C_2.[149] Due to the interaction between Na and CTAB, abundant nucleation sites for sodium were provided. Sodium directionally grows along the provided nucleation sites, achieving dendrite-free plating. These hybrid nanostructures

TABLE 4 Summary of the freestanding MXene-based macroforms for various batteries.

Materials	Devices	Performance	Ref.
f-Ti_3C_2	LIBs	410 mAh g^{-1} at 10 C	[74]
Al^{3+}-$Ti_3C_2T_x$	LIBs	~150 mAh g^{-1} at 1 C for 100 cycles	[122]
$Ti_3C_2T_x$/CTAB	Mg^{2+}-IBs	300 mAh cm^{-3} at 50 mA g^{-1}	[123]
3D $Ti_3C_2T_x$	SIBs	295 mAh g^{-1} at 2.5 C for 1000 cycles	[79]
3D Mo_2CT_x	SIBs	290 mAh g^{-1} at 2.5 C for 1000 cycles	[79]
3D V_2CT_x	SIBs	310 mAh g^{-1} at 2.5 C for 1000 cycles	[79]
PO_2-Nb_4C_3	SIBs	177 mAh g^{-1} at charging time of 4.9 min	[24]
S-doped $Ti_3C_2T_x$	SIBs	625.6 mAh cm^{-3} at 0.1 A g^{-1} over 5000 cycles	[124]
$Ti_3C_2Br_2$	ZIBs	120 mAh g^{-1} at 0.25 A g^{-1}	[126]
$Ti_3C_2I_2$	ZIBs	181 mAh g^{-1} at 0.25 A g^{-1}	[126]
Si/$Ti_3C_2T_x$	LIBs	1672 mAh g^{-1} at 1 A g^{-1} after 200 cycles	[127]
MnO_x@$Ti_3C_2T_x$	ZIBs	88 mAh g^{-1} at 0.1 A g^{-1}, 44 mAh g^{-1} at 10 A g^{-1}	[117]
CNT/Nb_2CT_x	LIBs	400 mAh g^{-1} at 0.5 C	[151]
$Ti3C_2$ MXene/CNT	SIBs	421 mAh cm^{-3} at 20 mA g^{-1}	[89]
Phosphorene/$Ti_3C_2T_x$	SIBs	343 mAh g^{-1} after 1000 cycles at 1 A g^{-1}	[118]
Ti_3C_2–rGO	LIBs	212.5 mAh g^{-1} after 1000 cycles at 1 A g^{-1}	[128]
Ti_3C2T_x foam/S	LiSBs	1226.4 mAh g^{-1} at 0.2 C after 1000 cycles	[129]
$Ti_3C_2T_x$/S	LiSBs	1075 mAh g^{-1} at 2 C with a capacity decay of 0.014% after 1500 cycles	[29]

(Continues)

consisting of 1D nanowires and the layered 2D MXene nanosheets effectively endowed the Na deposition, and the parallel MXene layers confined the nucleation in the nanochannels and along the surface, greatly inhibiting the dendrite growth. Alloy agents were verified to be efficient metal nucleation sites with reduced nucleation barriers, and thus they would guide the uniform metal nucleation and deposition. For instance, Tian et al.[150] produced uniform Sb arrays on MXene paper via electrodeposition and galvanic replacement strategies. Sb with the ability to form the ZnSb alloy not only served as seeds for even Zn nucleation but also worked as the electrochemically active Zn-storage material. Consequently, the MXene@Sb electrode achieved a long cycling life of 1000 h at 0.5 mA cm^{-2} with a dendrite-free morphology. The electrochemical performance of the freestanding MXene-based macroforms for various batteries is summarized in **Table 4**.

3.2 | MXene macroforms as electrode materials for supercapacitors

Due to the large specific surface area, abundant surface groups, and high electronic conductivity, MXenes have been widely demonstrated as superior supercapacitor electrode materials. Two-dimensional MXene nanosheets can be easily processed to fabricate freestanding electrodes due to their high dispersion ability in water and high

mechanical strength, showing a great potential application for flexible supercapacitors.[155,156] Ghidiu et al.[59] synthesized a flexible film made of hydrated $Ti_3C_2T_x$ using LiF and 6 M HCl. The clay-like $Ti_3C_2T_x$ was pressed between two roller mills to form a thin and free-standing film. The obtained freestanding $Ti_3C_2T_x$ film showed a volumetric capacitance of 900 F cm^{-3} (245 F g^{-1}) at 2 mV s^{-1} and stable cycling performance for 10 000 cycles at 10 A g^{-1} with the capacitance retention of ~100% in the 1 M H_2SO_4 electrolyte. Recently, Zhao et al.[35] proposed a method utilizing Zn foil to synchronously reduce and self-assemble the flexible $Ti_3C_2T_x$ MXene film. The negatively charged oxygen-containing functional groups on the surface of MXene sheets were reduced, and simultaneously a self-assembled cross-linked 3D network structure was formed (Figure 11A). The self-assembled MXene film depicted good mechanical properties at the macro-level and a uniform porous structure at the micro-level. Moreover, it showed the virtuous and excellent electrochemical performance in 1 M H_2SO_4 electrolyte (160 F g^{-1} at 500 mV s^{-1}). Meanwhile, the performance of the solid-state supercapacitor based on the MXene film was well maintained before and after the bending test.

Employing template or etching methods has been intensively used to improve the porosity of the MXene structure. Considering that vacuum filtration normally induces a densely stacked lamellar structure and impedes the charge transfer between layers, Lukatskaya et al.[157] added PMMA

TABLE 4 (Continued)

Materials	Devices	Performance	Ref.
S@V_2C MXene/rGO-CNT	LiSBs	1093 mAh g^{-1} at 0.2 C and per cycle 0.051% capacity decay at 2 C	[130]
3D VO_2(p)-V_2C/S	LiSBs	1250 mAh g^{-1} at 0.2 C	[152]
S/Oxi-d-$Ti_3C_2T_x$	LiSBs	900 mAh g^{-1} after 300 cycles at 1 C	[138]
TiO_2/H-$Ti_3C_2T_x$	LiSBs	740 mAh g^{-1} at 2 C and 95% capacity retention after 3500 cycles	[131]
N-Ti_3C_2/C	LiSBs	1332 mAh g^{-1} at 0.1 C	[153]
SA-Zn-MXene	LiSBs	1210 mAh g^{-1} at 0.2 C	[132]
$Ti_3C_2T_x$ MXene	LMBs	Lifespan over 1000 cycles with CE >99.0%	[148]
$Ti_3C_2T_x$ MXene@Zn	LMBs/ZMBs	Cycling stability at 2 mA cm^{-2} (for over 300 h)	[139]
$Ti_3C_2T_x$–CC	SMBs	Lifespan over 900 h at 5 mAh cm^{-2}	[140]
$Ti_3C_2T_x$@CNF	SMBs	Stability for over 1300 h at 0.5 mA cm^{-2}	[141]
DN-Ti_3CN-MXene/CNT	PMBs	Stable over 200 cycles at 5 mAh cm^{-2}	[142]
$Ti_3C_2T_x$ MXene@Sb	ZMBs	Cycling life of up to 1000 h at 0.5 mA cm^{-2}	[150]
S/MX@ZnS@Zn	ZMBs	Cycling stability up to 1600 at 0.5 mA cm^{-2}	[154]

Abbreviations: CC, carbon cloth; CNF, cellulose nanofiber; CNT, carbon nanotube; CTAB, cetyltrimethylammonium bromide; LIBs, lithium-ion batteries; LiSBs, lithium–sulfur batteries; LMBs, lithium metal batteries; PMBs, potassium metal batteries; rGO, reduced graphene oxide; SA, surface absorption; SIBs, sodium-ion batteries; SMBs, sodium metal batteries; ZIBs, zinc-ion batteries; ZMBs, zinc metal batteries.
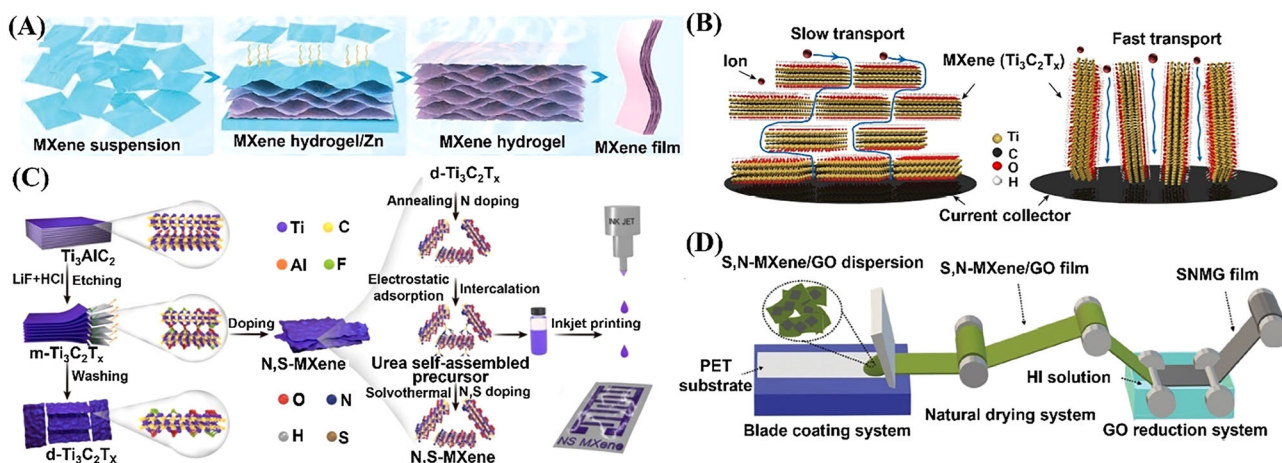
FIGURE 11 (A) Illustration showing the reduction process of MXene by Zn foil. Reproduced with permission.[35] Copyright 2021, Wiley-VCH. (B) Illustration showing different ion transport channels of the laterally stacked MXene film and the vertically aligned MXene film. Reproduced with permission.[38] Copyright 2018, Springer Nature. (C) Schematic illustration showing the inkjet-printed N, S-MXene-based MSCs. Reproduced with permission.[155] Copyright 2022, Elsevier. (D) Illustration showing the fabrication process of S, N-MXene/rGO film. Reproduced with permission.[85] Copyright 2021, Wiley-VCH. rGO, reduced graphene oxide.

microspheres as the template to construct the porous $Ti_3C_2T_x$ MXene film. The prepared MXene film showed an open porous structure, which improved the ion accessibility to the redox-active sites. As a result, a specific capacitance of 380 F g^{-1} at 2 mV s^{-1} was achieved by the prepared $Ti_3C_2T_x$ MXene film in the 3 M H_2SO_4 electrolyte. Besides, Tang et al.[158] fabricated $Ti_3C_2T_x$ with a porous structure through a chemical etching process with concentrated H_2SO_4. $Ti_3C_2T_x$ nanosheets were partially etched without destroying the crystal structure of the unetched part. At the same time, the interlayer spacing of $Ti_3C_2T_x$

obviously expanded at the atomic level due to oxidation. The assembled film made of porous $Ti_3C_2T_x$ nanosheets with the increased interlayer spacing enabled a fast and interconnected ion transport pathway. As a result, the $Ti_3C_2T_x$ film with a loading of 0.4 mg cm^{-2} (thickness, 1.1 μm) showed an ultrahigh rate capability (i.e., 208 F g^{-1}, 756 F cm^{-3} at 10 V s^{-1}) in 3 M H_2SO_4. It also demonstrated excellent potential for practical applications at high loading. Recently, Yang and coworkers[38] reported vertically aligned 2D $Ti_3C_2T_x$ flakes via a self-assembly method. The vertical alignment endowed fast directional ion transport,

which is highly desired for fast energy storage. In contrast, the laterally stacked $Ti_3C_2T_x$ MXene film showed long and twisted channels for ion transport (Figure 11B). In vertically aligned $Ti_3C_2T_x$ MXene film, most $Ti_3C_2T_x$ MXene nanosheets were vertically aligned on the current collector. The vertical $Ti_3C_2T_x$ MXene-based electrode exhibited superior electrochemical performance to a stacked microporous $Ti_3C_2T_x$ MXene electrode. Only a slight decrease in the rate performance was revealed, when the film thickness was increased from 40 to 200 μm.

In order to improve the electrochemical performance of MXene for supercapacitor applications, heteroatom doping (including N, P, and S) is a feasible research direction. Chemical doping can improve the electrochemical performance of MXene by regulating the electron transport process. [84,155,159] Tian et al.[159] synthesized O-doped $Ti_3C_2T_x$ MXene nanosheet by etching O-doped Ti_3AlC_2 MAX phases with O substitution of C atoms. The introduction of appropriate oxygen atoms could effectively enlarge the interlayer spacing, promote the –O termination formation from –OH, improve interface charge transfer, and enhance the interface capacitance. Consequently, a high capacity of 360.0 C g^{-1} at 5 mV s^{-1} was achieved for $Ti_3C_2T_x$ film in supercapacitors. Wei et al.[84] reported the in situ phosphorus doping at a low temperature by utilizing sodium hypophosphite as the phosphorus source. Phosphorus doping was proven to generate P–O and P–C bonds in $Ti_3C_2T_x$, which increased the interlayer spacing of $Ti_3C_2T_x$ from 12.87 to 13.87 Å. This allowed an efficient path for electrolyte ions to migrate into the electrode and also provided rich active sites for pseudocapacitive charge storage. As a result, P-doped $Ti_3C_2T_x$ showed an improved capacitance of 476.9 F g^{-1} at 2 mV s^{-1} as compared to that of $Ti_3C_2T_x$ (344.4 F g^{-1}). Furthermore, Sun et al.[155] fabricated N, S-$Ti_3C_2T_x$ MXene ink for inkjet printing microsupercapacitors (Figure 11C). Nitrogen and sulfur dopants were introduced by annealing treatment under N_2 atmosphere and solvothermal treatment with thiourea. DFT calculations were conducted to explore the electrochemical reaction mechanism of N, S-MXene, which can facilitate the electron transfer due to superior metallicity and improve the H$^+$ adsorption due to the lower H$^+$ adsorption energy of N, S, O in N, S-$Ti_3C_2T_x$ (−1.55, 0.37, −0.48 eV). Impressively, the N, S-MXene film exhibited an excellent volumetric capacitance of 710 F cm^{-3} at 20 μA cm^{-2} and good cycling stability (i.e., 94.6% capacitance retention after 10 000 cycles at 100 μA cm^{-2}) in the 3 M H_2SO_4 electrolyte.

Hybridization with other materials has also been widely used to improve the electrochemical performance of MXenes for supercapacitors. Levitt et al.[160] prepared the freestanding MXene $Ti_3C_2T_x$/carbon nanofiber hybrid by carbonizing the electrospun MXene/PAN fibers. MXene flakes were embedded within carbon nanofibers with a content of up to 35 wt%. An areal capacitance of 205 mF cm^{-2} at 50 mV s^{-1} was achieved by the freestanding $Ti_3C_2T_x$/carbon nanofiber hybrid with 10 wt% MXene in the 1 M H_2SO_4 electrolyte. Besides, Liu and coworkers[85] reported an industry-scale and environmentally stable S, N-MXene/rGO film for supercapacitors. The fabrication processes included the blade coating process, natural drying process, and GO reduction process (Figure 11D). Due to $\pi-\pi$ stacking interactions between the rGO sheets and S, N-MXene/rGO film with 40 wt% rGO demonstrated a high mechanical strength (≈45 MPa) and high electron conductivity (≈1200 S cm^{-1}). More importantly, the fabricated film exhibited a high volumetric capacitance of 698.5 F cm^{-3} at 1 A g^{-1} and excellent cycling stability (i.e., capacitance retention of 98% after 30 000 cycles at 100 mV s^{-1}). Furthermore, Li et al.[161] proposed an all-MXene hybrid film for supercapacitors. Few-layer Nb_2CT_x and $Ti_3C_2T_x$ nanosheets were first synthesized at the lower reaction temperature and shorter reaction time. Afterward, the Nb_2CT_x/$Ti_3C_2T_x$ hybrid films were fabricated with vacuum filtration. The obtained thin film effectively avoided the stacking of MXene nanosheets, and the interconnected nanosheet served as a fast electron conductive network. Consequently, the $Ti_3C_2T_x$/Nb_2CT_x film showed a specific capacitance of 370 F g^{-1} at 2 mV s^{-1} and the capacitance retention of 56.1% at 200 mV s^{-1}. Moreover, Bin et al.[162] demonstrated an N-doped d-$Ti_3C_2T_x$/MoO film for supercapacitors. Layer-structured 2D N-doped d-$Ti_3C_2T_x$ material acted as a conductive current collector and provided sufficient ion transport channels. Meanwhile, homogeneous MoO nanoparticles grown on the surface of the d-$Ti_3C_2T_x$ nanosheets effectively avoided the interlayer rearrangement of nanosheets, increased the available active sites for redox reactions, and facilitated electron transport and ion diffusion. As a result, the N-d-$Ti_3C_2T_x$/MoO$_x$ film demonstrated a specific capacitance of 341.0 F g^{-1} at 2 mV s^{-1} and the capacitance retention of 99.2% after 11 000 cycles at 5 A g^{-1}. The electrochemical performance of freestanding MXene macroforms for supercapacitor applications is summarized in **Table 5**.

4 | SUMMARY AND PERSPECTIVES

Due to their exceptional electronic conductivity, abundant surface functional groups, and impressive mechanical strength, MXene-based macroforms have gained significant attention in the field of electrochemical energy storage devices. Various strategies have been employed to further enhance their electrochemical performance for application in batteries and supercapacitors. These strategies include interlayer intercalation, vertical alignment

TABLE 5 Summary of freestanding MXene macroforms for supercapacitors.

Materials	Electrolyte	Specific capacitance	Cycling stability	Ref.
MXene film	1 M H_2SO_4	900 F cm^{-3} at 2 mV s^{-1}	~100% (10 000 cycles)	59
MXene film via Zn foil reduction	1 M H_2SO_4	296 F g^{-1} at 2 mV s^{-}		1–35
PMMA-template MXene film	3 M H_2SO_4	380 F g^{-1} at 2 mV s^{-1}	90% (10 000 cycles)	157
MXene film	3 M H_2SO_4	327 F g^{-1} at 5 mV s^{-1}	99.3% (10 000 cycles)	
Vertical alignment MXene	3 M H_2SO_4	>200 F g^{-1} at 2 V s^{-1}	~100% (10 000 cycles)	38
O-doped MXene	3 M H_2SO_4	306 C g^{-1} at 5 mV s^{-}		1–159
N, S-doped MXene	3 M H_2SO_4	266 F g^{-1} at 1 A g^{-1}	94.6% (10 000 cycles)	155
P-doped MXene	3 M H_2SO_4	476.9 F g^{-1} at 2 mV s^{-1}	97.6% (8000 cycles)	84
MXene/CNFs	1 M H_2SO_4	239 mF cm^{-2} at 10 mV s^{-1}	~100% (100 000 cycles)	160
N-doped porous MXene/TiO$_2$	LiCl/PVA	918.69 F g^{-1} at 0.5 A g^{-1}	74.39% (10 000 cycles)	163
N-doped Ti$_3$C$_2$T$_x$/MoO$_x$	3 M H_2SO_4	487.1 F g^{-1} at 2 mV s^{-1}	99.2% (11 000 cycles)	162
MXene/holey graphene	3 M H_2SO_4	1445 F cm^{-3} at 2 mV s^{-1}	93% (10 000 cycles)	43
MXene/rGO film	3 M H_2SO_4	1040 F cm^{-3} at 2 mV s^{-1}	~100% (20 000 cycles)	93
MXene/rGO	PVA-H_2SO_4	140 F g^{-1} at 0.5 A g^{-1}	85% (10 000 cycles)	164
N, S-MXene/rGO	1 M H_2SO_4	698.5 F cm^{-3} at 1 A g^{-1}	98% (30 000 cycles)	85
Nb$_2$CT$_x$/Ti$_3$C$_2$T$_x$	2 M H_2SO_4	370 F g^{-1} at 2 mV s^{-1}	94% (10 000 cycles)	161

Abbreviations: CNF, cellulose nanofiber; PMMA, polymethyl methacrylate; PVA, poly(vinyl alcohol), rGO, reduced graphene oxide.

design, heteroatom doping, and hybridization with guest materials. These approaches have shown promising results in improving the functionality of MXene-based macroforms for energy storage applications. However, despite the remarkable progress made, there are still certain remaining challenges that need to be addressed in further research. These challenges include issues related to stability, scalability, long-term cycling performance, and the integration of MXene macroforms into practical device architectures. By focusing on these challenges and exploring potential solutions, future work can further advance the field of MXene-based macroforms for electrochemical energy storage.

1. Most studies have focused on Ti$_3$C$_2$T$_x$ MXenes, but it is crucial to synthesize and investigate other MXenes with high stability and favorable electrochemical properties. Computational material science can play a key role in efficiently screening materials for high-performance MXene electrodes, utilizing the vast amounts of data available. Furthermore, there is a strong emphasis on developing large-scale synthesis methods for MXenes using environmentally friendly green chemistry approaches.

2. The reactivity of MXene nanosheets toward dissolved oxygen in water limits their processability, which is a critical factor for the fabricating freestanding MXene-based macroforms. Improving the processability of MXene nanosheets is necessary, and optimizing the solution processing parameters for large-scale pro-

duction of high-quality MXene-based macroforms is essential.

3. While various strategies such as intercalation, surface functional group modification, and hybridization have been explored, each strategy has its own imitations. Therefore, a systematic approach that combines the advantages of different strategies holds greater promise in enhancing MXene performance.

4. It is imperative to fully understand the charge storage mechanism of modified MXenes through experimental and theoretical investigation during electrochemical reactions. Fundamental studies on the interaction between MXenes and metal ions/polysulfides are crucial. Additionally, studying the chemical and structural stability of modified MXenes over long-term cycling is essential for their practical application.

5. The mechanical strength of freestanding MXene electrodes is currently insufficient to meet the stringent requirements of flexible devices due to weak inter-sheet interactions. While hybridization with other materials can improve mechanical properties, it may also lead to a decrease in overall energy density due to the introduction of non-active components. Balancing mechanical strength and energy density remains a challenge in the development of freestanding MXene electrodes.

6. The exploration of suitable geometric design strategies is vital for enhancing robust flexibility and stretchability in MXene-based macroforms. The creation of undulating or wave-like structures, as well as "origami" and "kirigami" inspired structures may push the boundaries

of conventional flexibility and stretchability parameters.

CONFLICT OF INTEREST STATEMENT

The authors declare no conflict of interest.

ORCID

Qiongqiong Lu https://orcid.org/0000-0001-6998-6275

REFERENCES

1. Chu S, Cui Y, Liu N. The path towards sustainable energy. *Nat Mater*. 2017;16(1):16-22.
2. Kebede AA, Kalogiannis T, Van Mierlo J, Berecibar M. A comprehensive review of stationary energy storage devices for large scale renewable energy sources grid integration. *Renew Sustain Energy Rev*. 2022;159:112213.
3. Dong Y, Lu P, Ding Y, Shi H, Feng X, Wu Z-S. Advanced design of cathodes and interlayers for high-performance lithium-selenium batteries. *SusMat*. 2021;1(3):393-412.
4. Liu L, Wang J, Oswald S, et al. Decoding of oxygen network distortion in a layered high-rate anode by in situ investigation of a single microelectrode. *ACS Nano*. 2020;14(9):11753-11764.
5. Xiang X, Lu Q, Han M, Chen J. Superior high-rate capability of $Na_3(VO_{0.5})_2(PO_4)_2F_2$ nanoparticles embedded in porous graphene through the pseudocapacitive effect. *Chem Comm*. 2016;52(18):3653-3656.
6. Liu Y, Hu J, Lu Q, et al. Highly enhanced reversibility of a Zn anode by in-situ texturing. *Energy Storage Mater*. 2022;47:98-104.
7. Lu Q, Wang X, Cao J, et al. Freestanding carbon fiber cloth/sulfur composites for flexible room-temperature sodium-sulfur batteries. *Energy Storage Mater*. 2017;8:77-84.
8. Lu Q, Omar A, Ding L, et al. A facile method to stabilize sodium metal anodes towards high-performance sodium batteries. *J Mater Chem A*. 2021;9(14):9038-9047.
9. Wang Z, Zhou M, Qin L, et al. Simultaneous regulation of cations and anions in an electrolyte for high-capacity, high-stability aqueous zinc–vanadium batteries. *eScience*. 2022;2(2):209-218.
10. Morag A, Yu M. Layered electrode materials for non-aqueous multivalent metal batteries. *J Mater Chem A*. 2021;9(35):19317-19345.
11. Liu L, Niu Z, Chen J. Unconventional supercapacitors from nanocarbon-based electrode materials to device configurations. *Chem Soc Rev*. 2016;45(15):4340-4363.
12. Wang X, Lu Q, Chen C, et al. A consecutive spray printing strategy to construct and integrate diverse supercapacitors on various substrates. *ACS Appl Mater Interfaces*. 2017;9(34):28612-28619.
13. Chen C, Cao J, Lu Q, et al. Foldable all-solid-state supercapacitors integrated with photodetectors. *Adv Funct Mater*. 2017;27(3):1604639.
14. Chen K, Cao J, Lu Q, et al. Sulfur nanoparticles encapsulated in reduced graphene oxide nanotubes for flexible lithium–sulfur batteries. *Nano Res*. 2018;11(3):1345-1357.
15. Du Y-H, Liu X-Y, Wang X-Y, et al. Freestanding strontium vanadate/carbon nanotube films for long-life aqueous zinc-ion batteries. *Rare Metals*. 2022;41(2):415-424.
16. Cao J, Chen C, Zhao Q, et al. A flexible nanostructured paper of a reduced graphene oxide–sulfur composite for high-performance lithium–sulfur batteries with unconventional configurations. *Adv Mater*. 2016;28(43):9629.
17. Lu Q, Jie Y, Meng X, et al. Carbon materials for stable Li metal anodes: challenges, solutions, and outlook. *Carbon Energy*. 2021;3(6):957-975.
18. Li X, Huang Z, Shuck CE, Liang G, Gogotsi Y, Zhi C. MXene chemistry, electrochemistry and energy storage applications. *Nat Rev Chem*. 2022;6:389-404.
19. Dong Y, Shi H, Wu Z-S. Recent advances and promise of MXene-based nanostructures for high-performance metal ion batteries. *Adv Funct Mater*. 2020;30(47):2000706.
20. Hong W, Wyatt BC, Nemani SK, Anasori B. Double transition-metal MXenes: atomistic design of two-dimensional carbides and nitrides. *MRS Bull*. 2020;45(10):850-861.
21. Naguib M, Kurtoglu M, Presser V, et al. Two-dimensional nanocrystals produced by exfoliation of Ti_3AlC_2. *Adv Mater*. 2011;23(37):4248.
22. Huang Y, Lu Q, Wu D, et al. Flexible MXene films for batteries and beyond. *Carbon Energy*. 2022;4(4):598-620.
23. Mathis TS, Maleski K, Goad A, et al. Modified max phase synthesis for environmentally stable and highly conductive Ti_3C_2 MXene. *ACS Nano*. 2021;15(4):6420-6429.
24. Sun B, Lu Q, Chen K, et al. Redox-active metaphosphate-like terminals enable high-capacity MXene anodes for ultrafast Na-ion storage. *Adv Mater*. 2022;34(15):2108682.
25. Wu Z, Shang T, Deng Y, Tao Y, Yang Q-H. The assembly of MXenes from 2D to 3D. *Adv Sci*. 2020;7(7):1903077.
26. Xiong D, Shi Y, Yang HY. Rational design of MXene-based films for energy storage: progress, prospects. *Mater Today*. 2021;46:183-211.
27. Lipton J, Röhr JA, Dang V, et al. Scalable, highly conductive, and micropatternable MXene films for enhanced electromagnetic interference shielding. *Matter*. 2020;3(2):546-557.

28. Zhang T, Zhang L, Hou Y. MXenes: synthesis strategies and lithium–sulfur battery applications. *eScience*. 2022;2(2):164-182.

29. Tang H, Li W, Pan L, et al. A robust, freestanding MXene-sulfur conductive paper for long-lifetime Li–S batteries. *Adv Funct Mater*. 2019;29(30):1901907.

30. Zhang X, Lv R, Wang A, Guo W, Liu X, Luo J. MXene aerogel scaffolds for high-rate lithium metal anodes. *Angew Chem Int Ed*. 2018;57(46):15028-15033.

31. Levitt A, Zhang J, Dion G, Gogotsi Y, Razal JM. MXene-based fibers, yarns, and fabrics for wearable energy storage devices. *Adv Funct Mater*. 2020;30(47):2000739.

32. Zhang P, Wang F, Yang S, Wang G, Yu M, Feng X. Flexible in-plane micro-supercapacitors: progresses and challenges in fabrication and applications. *Energy Storage Mater*. 2020;28:160-187.

33. Yu M, Feng X. Thin-film electrode-based supercapacitors. *Joule*. 2019;3(2):338-360.

34. Zhang J, Uzun S, Seyedin S, et al. Additive-free MXene liquid crystals and fibers. *ACS Cent Sci*. 2020;6(2):254-265.

35. Zhao Z, Wang S, Wan F, Tie Z, Niu Z. Scalable 3D self-assembly of MXene films for flexible sandwich and microsized supercapacitors. *Adv Funct Mater*. 2021;31(23):2101302.

36. Bian R, He G, Zhi W, Xiang S, Wang T, Cai D. Ultralight MXene-based aerogels with high electromagnetic interference shielding performance. *J Mater Chem C*. 2019;7(3):474-478.

37. Luo J, Zhang W, Yuan H, et al. Pillared structure design of MXene with ultralarge interlayer spacing for high-performance lithium-ion capacitors. *ACS Nano*. 2017;11(3):2459-2469.

38. Xia Y, Mathis TS, Zhao M-Q, et al. Thickness-independent capacitance of vertically aligned liquid-crystalline MXenes. *Nature*. 2018;557(7705):409-412.

39. Zhu Y, Rajouâ K, Le Vot S, Fontaine O, Simon P, Favier F. Modifications of MXene layers for supercapacitors. *Nano Energy*. 2020;73:104734.

40. Hu M, Cheng R, Li Z, et al. Interlayer engineering of $Ti_3C_2T_x$ MXenes towards high capacitance supercapacitors. *Nanoscale*. 2020;12(2):763-771.

41. Bao W, Shuck CE, Zhang W, Guo X, Gogotsi Y, Wang G. Boosting performance of Na–S batteries using sulfur-doped $Ti_3C_2T_x$ MXene nanosheets with a strong affinity to sodium polysulfides. *ACS Nano*. 2019;13(10):11500-11509.

42. Wang T, Shen D, Liu H, Chen H, Liu Q, Lu B. A Sb_2S_3 nanoflower/MXene composite as an anode for potassium-ion batteries. *ACS Appl Mater Interfaces*. 2020;12(52):57907-57915.

43. Fan Z, Wang Y, Xie Z, et al. Modified MXene/holey graphene films for advanced supercapacitor electrodes with superior energy storage. *Adv Sci*. 2018;5(10):1800750.

44. Boota M, Anasori B, Voigt C, Zhao M-Q, Barsoum MW, Gogotsi Y. Pseudocapacitive electrodes produced by oxidant-free polymerization of pyrrole between the layers of 2D titanium carbide (MXene). *Adv Mater*. 2016;28(7):1517-1522.

45. Li T, Yao L, Liu Q, et al. Fluorine-free synthesis of high-purity Ti_3C2T_x (T = OH, O) via alkali treatment. *Angew Chem Int Ed*. 2018;57(21):6115-6119.

46. Li Y, Shao H, Lin Z, et al. A general Lewis acidic etching route for preparing MXenes with enhanced electrochemical performance in non-aqueous electrolyte. *Nat Mater*. 2020;19(8):894-899.

47. Yang S, Zhang P, Wang F, et al. Fluoride-free synthesis of two-dimensional titanium carbide (MXene) using a binary aqueous system. *Angew Chem Int Ed*. 2018;57(47):15491-15495.

48. Abdolhosseinzadeh S, Heier J, Zhang C. Printing and coating MXenes for electrochemical energy storage devices. *J Phys Energy*. 2020;2(3):031004.

49. Alhabeb M, Maleski K, Anasori B, et al. Guidelines for synthesis and processing of two-dimensional titanium carbide ($Ti_3C_2T_x$ MXene). *Chem Mater*. 2017;29(18):7633-7644.

50. Meng W, Liu X, Song H, et al. Advances and challenges in 2D MXenes: from structures to energy storage and conversions. *Nano Today*. 2021;40:101273.

51. Halim J, Palisaitis J, Lu J, et al. Synthesis of two-dimensional $Nb_{1.33}C$ (MXene) with randomly distributed vacancies by etching of the quaternary solid solution $(Nb_{2/3}Sc_{1/3})_2AlC$ max phase. *ACS Appl Nano Mater*. 2018;1(6):2455-2460.

52. Dai C, Chen Y, Jing X, et al. Two-dimensional tantalum carbide (MXenes) composite nanosheets for multiple imaging-guided photothermal tumor ablation. *ACS Nano*. 2017;11(12):12696-12712.

53. Meshkian R, Näslund L-Å, Halim J, Lu J, Barsoum MW, Rosen J. Synthesis of two-dimensional molybdenum carbide, Mo_2C, from the gallium based atomic laminate Mo_2Ga_2C. *Scr Mater*. 2015;108:147-150.

54. Li X, Li M, Yang Q, et al. Phase transition induced unusual electrochemical performance of V_2CT_x MXene for aqueous zinc hybrid-ion battery. *ACS Nano*. 2020;14(1):541-551.

55. Naguib M, Halim J, Lu J, et al. New two-dimensional niobium and vanadium carbides as promising materials for Li-ion batteries. *J Am Chem Soc*. 2013;135(43):15966-15969.

56. Meshkian R, Dahlqvist M, Lu J, et al. W-based atomic laminates and their 2D derivative $W_{1.33}C$ MXene with vacancy ordering. *Adv Mater*. 2018;30(21):1706409.

57. Zhou J, Zha X, Chen FY, et al. A two-dimensional zirconium carbide by selective etching of Al_3C_3 from nanolaminated $Zr_3Al_3C_5$. *Angew Chem Int Ed*. 2016;55(16):5008-5013.

58. Zhou J, Zha X, Zhou X, et al. Synthesis and electrochemical properties of two-dimensional hafnium carbide. *ACS Nano*. 2017;11(4):3841-3850.

59. Ghidiu M, Lukatskaya MR, Zhao M-Q, Gogotsi Y, Barsoum MW. Conductive two-dimensional titanium carbide 'clay' with high volumetric capacitance. *Nature*. 2014;516(7529):78-81.

60. Wang L, Zhang H, Wang B, et al. Synthesis and electrochemical performance of $Ti_3C_2T_x$ with hydrothermal process. *Electron Mater Lett*. 2016;12(5):702-710.

61. Soundiraraju B, George BK. Two-dimensional titanium nitride (Ti_2N) MXene: synthesis, characterization, and potential application as surface-enhanced Raman scattering substrate. *ACS Nano*. 2017;11(9):8892-8900.

62. Halim J, Kota S, Lukatskaya MR, et al. Synthesis and characterization of 2D molybdenum carbide (MXene). *Adv Funct Mater*. 2016;26(18):3118-3127.

63. Ma G, Shao H, Xu J, et al. Li-ion storage properties of two-dimensional titanium-carbide synthesized via fast one-pot method in air atmosphere. *Nat Commun*. 2021;12(1):5085.

64. Urbankowski P, Anasori B, Makaryan T, et al. Synthesis of two-dimensional titanium nitride Ti_4N_3 (MXene). *Nanoscale*. 2016;8(22):11385-11391.

65. Dong H, Xiao P, Jin N, Wang B, Liu Y, Lin Z. Molten salt derived Nb_2CT_x MXene anode for Li-ion batteries. *ChemElectroChem*. 2021;8(5):957-962.

66. Li X, Li M, Yang Q, et al. In situ electrochemical synthesis of MXenes without acid/alkali usage in/for an aqueous zinc ion battery. *Adv Energy Mater*. 2020;10(36):2001791.

67. Sun W, Shah SA, Chen Y, et al. Electrochemical etching of Ti_2AlC to Ti_2CT_x (MXene) in low-concentration hydrochloric acid solution. *J Mater Chem*. 2017;5(41):21663-21668.

68. Yang S, Zhang P, Nia AS, Feng X. Emerging 2D materials produced via electrochemistry. *Adv Mater*. 2020;32(10):1907857.

69. Xu C, Wang L, Liu Z, et al. Large-area high-quality 2D ultrathin Mo_2C superconducting crystals. *Nat Mater*. 2015;14(11):1135-1141.

70. Wang D, Zhou C, Filatov AS, et al. Direct synthesis and chemical vapor deposition of 2D carbide and nitride MXenes. *Science*. 2023;379(6638):1242-1247.

71. Zhang F, Zhang Z, Wang H, et al. Plasma-enhanced pulsed-laser deposition of single-crystalline Mo_2C ultrathin superconducting films. *Phys Rev Mater*. 2017;1(3):034002.

72. Shinde PA, Patil AM, Lee S, Jung E, Jun SC. Two-dimensional MXenes for electrochemical energy storage applications. *J Mater Chem A*. 2022;10(3):1105-1149.

73. Zhang CJ, Pinilla S, McEvoy N, et al. Oxidation stability of colloidal two-dimensional titanium carbides (MXenes). *Chem Mater*. 2017;29(11):4848-4856.

74. Mashtalir O, Naguib M, Mochalin VN, et al. Intercalation and delamination of layered carbides and carbonitrides. *Nat Commun*. 2013;4(1):1716.

75. Mashtalir O, Lukatskaya MR, Kolesnikov AI, et al. The effect of hydrazine intercalation on the structure and capacitance of 2D titanium carbide (MXene). *Nanoscale*. 2016;8(17):9128-9133.

76. Li K, Wang X, Li S, et al. An ultrafast conducting polymer@MXene positive electrode with high volumetric capacitance for advanced asymmetric supercapacitors. *Small*. 2020;16(4):1906851.

77. Tang J, Huang X, Qiu T, et al. Interlayer space engineering of MXenes for electrochemical energy storage applications. *Chem Eur J*. 2021;27(6):1921-1940.

78. Wang Y, Wang X, Li X, et al. Engineering 3D ion transport channels for flexible MXene films with superior capacitive performance. *Adv Funct Mater*. 2019;29(14):1900326.

79. Zhao M-Q, Xie X, Ren CE, et al. Hollow MXene spheres and 3D macroporous MXene frameworks for Na-ion storage. *Adv Mater*. 2017;29(37):1702410.

80. Ren CE, Zhao M-Q, Makaryan T, et al. Porous two-dimensional transition metal carbide (MXene) flakes for high-performance Li-ion storage. *ChemElectroChem*. 2016;3(5):689-693.

81. Cui Y, Xie X, Yang R, Qin J, Zheng L, Cao M. Cold pressing-built microreactors to thermally manipulate microstructure of MXene film as an anode for high-performance lithium-ion batteries. *Electrochim Acta*. 2019;305:11-23.

82. Fan Z, Wei C, Yu L, et al. 3D printing of porous nitrogen-doped Ti_3C_2 MXene scaffolds for high-performance sodium-ion hybrid capacitors. *ACS Nano*. 2020;14(1):867-876.

83. Lu C, Yang L, Yan B, et al. Nitrogen-doped Ti_3C_2 MXene: mechanism investigation and electrochemical analysis. *Adv Funct Mater*. 2020;30(47):2000852.

84. Wei X, Cai M, Yuan F, et al. The surface functional modification of $Ti_3C_2T_x$ MXene by phosphorus doping and its application in quasi-solid state flexible supercapacitor. *Appl Surf Sci*. 2022;606:154817.

85. Liao L, Jiang D, Zheng K, Zhang M, Liu J. Industry-scale and environmentally stable $Ti_3C_2T_x$ MXene based film for flexible energy storage devices. *Adv Funct Mater*. 2021;31(35):2103960.

86. Yang C, Tang Y, Tian Y, et al. Flexible nitrogen-doped 2D titanium carbides (MXene) films constructed by an ex situ solvothermal method with extraordinary volumetric capacitance. *Adv Energy Mater*. 2018;8(31):1802087.

87. Tian Y, Yang C, Que W, Liu X, Yin X, Kong LB. Flexible and free-standing 2D titanium carbide film decorated with manganese oxide nanoparticles as a high volumetric capacity electrode for supercapacitor. *J Power Sources*. 2017;359:332-339.

88. Tang J, Peng X, Lin T, Huang X, Luo B, Wang L. Confining ultrafine tin monophosphide in $Ti_3C_2T_x$ interlayers for rapid and stable sodium ion storage. *eScience*. 2021;1(2):203-211.

89. Xie X, Zhao M-Q, Anasori B, et al. Porous heterostructured MXene/carbon nanotube composite paper with high volumetric capacity for sodium-based energy storage devices. *Nano Energy*. 2016;26:513-523.

90. Zhao M-Q, Ren CE, Ling Z, et al. Flexible MXene/carbon nanotube composite paper with high volumetric capacitance. *Adv Mater*. 2015;27(2):339-345.

91. Fu Q, Wang X, Zhang N, et al. Self-assembled $Ti_3C_2T_x$/SCNT composite electrode with improved electrochemical performance for supercapacitor. *J Colloid Interface Sci*. 2018;511:128-134.

92. Li H, Chen R, Ali M, Lee H, Ko MJ. In situ grown MWCNTs/MXenes nanocomposites on carbon cloth for high-performance flexible supercapacitors. *Adv Funct Mater*. 2020;30(47):2002739.

93. Yan J, Ren CE, Maleski K, et al. Flexible MXene/graphene films for ultrafast supercapacitors with outstanding volumetric capacitance. *Adv Funct Mater*. 2017;27(30):1701264.

94. Zhang C, Wang L, Lei W, et al. Achieving quick charge/discharge rate of $3.0\,V\,s^{-1}$ by 2D titanium carbide (MXene) via N-doped carbon intercalation. *Mater Lett*. 2019;234:21-25.

95. Zhao T, Zhang J, Du Z, Liu Y, Zhou G, Wang J. Dopamine-derived N-doped carbon decorated titanium carbide composite for enhanced supercapacitive performance. *Electrochim Acta*. 2017;254:308-319.

96. Ling Z, Ren CE, Zhao M-Q, et al. Flexible and conductive MXene films and nanocomposites with high capacitance. *Proc Natl Acad Sci U S A*. 2014;111(47):16676-16681.

97. Wu W, Wei D, Zhu J, et al. Enhanced electrochemical performances of organ-like Ti_3C_2 MXenes/polypyrrole composites as supercapacitors electrode materials. *Ceram Int*. 2019;45(6):7328-7337.

98. Le TA, Tran NQ, Hong Y, Lee H. Intertwined titanium carbide MXene within a 3 D tangled polypyrrole nanowires matrix for enhanced supercapacitor performances. *Chem Eur J*. 2019;25(4):1037-1043.

99. Tang Y, Zhu J, Yang C, Wang F. Enhanced supercapacitive performance of manganese oxides doped two-dimensional titanium carbide nanocomposite in alkaline electrolyte. *J Alloys Compd*. 2016;685:194-201.

100. Fan Z, Wang Y, Xie Z, et al. A nanoporous MXene film enables flexible supercapacitors with high energy storage. *Nanoscale*. 2018;10(20):9642-9652.

101. Chen C, Xie X, Anasori B, et al. MoS_2-on-MXene heterostructures as highly reversible anode materials for lithium-ion batteries. *Angew Chem Int Ed*. 2018;57(7):1846-1850.

102. Wu Y, Nie P, Wu L, Dou H, Zhang X. 2D MXene/SnS_2 composites as high-performance anodes for sodium ion batteries. *Chem Eng J*. 2018;334:932-938.

103. Zhu M, Huang Y, Deng Q, et al. Highly flexible, freestanding supercapacitor electrode with enhanced performance obtained by hybridizing polypyrrole chains with MXene. *Adv Energy Mater*. 2016;6(21):1600969.

104. Wang J, Kang H, Ma H, et al. Super-fast fabrication of MXene film through a combination of ion induced gelation and vacuum-assisted filtration. *Eng Sci*. 2021;15:57-66.

105. Zhang J, Jiang D, Liao L, Cui L, Zheng R, Liu J. $Ti_3C_2T_x$ MXene based hybrid electrodes for wearable supercapacitors with varied deformation capabilities. *Chem Eng J*. 2022;429:132232.

106. Zhang J, Kong N, Uzun S, et al. Scalable manufacturing of free-standing, strong $Ti_3C_2T_x$ MXene films with outstanding conductivity. *Adv Mater*. 2020;32(23):2001093.

107. Yang W, Yang J, Byun JJ, et al. 3D printing of freestanding MXene architectures for current-collector-free supercapacitors. *Adv Mater*. 2019;31(37):1902725.

108. Kong J, Yang H, Guo X, et al. High-mass-loading porous $Ti_3C_2T_x$ films for ultrahigh-rate pseudocapacitors. *ACS Energy Lett*. 2020;5(7):2266-2274.

109. Li L, Zhang M, Zhang X, Zhang Z. New Ti_3C_2 aerogel as promising negative electrode materials for asymmetric supercapacitors. *J Power Sources*. 2017;364:234-241.

110. Fan Z, Wang D, Yuan Y, et al. A lightweight and conductive MXene/graphene hybrid foam for superior electromagnetic interference shielding. *Chem Eng J*. 2020;381:122696.

111. Ma Y, Yue Y, Zhang H, et al. 3D synergistical MXene/reduced graphene oxide aerogel for a piezoresistive sensor. *ACS Nano*. 2018;12(4):3209-3216.

112. Hu K, Wang H, Zhang X, et al. Ultralight $Ti_3C_2T_x$ MXene foam with superior microwave absorption performance. *Chem Eng J*. 2021;408:127283.

113. Shang T, Lin Z, Qi C, et al. 3D macroscopic architectures from self-assembled MXene hydrogels. *Adv Funct Mater*. 2019;29(33):1903960.

114. Deng Y, Shang T, Wu Z, et al. Fast gelation of $Ti_3C_2T_x$ MXene initiated by metal ions. *Adv Mater*. 2019;31(43):1902432.

115. Peng Y-Y, Akuzum B, Kurra N, et al. All-MXene (2D titanium carbide) solid-state microsupercapacitors for on-chip energy storage. *Energy Environ Sci*. 2016;9(9):2847-2854.

116. Pang J, Chang B, Liu H, Zhou W. Potential of MXene-based heterostructures for energy conversion and storage. *ACS Energy Lett*. 2022;7(1):78-96.

117. Luo S, Xie L, Han F, et al. Nanoscale parallel circuitry based on interpenetrating conductive assembly for flexible and high-power zinc ion battery. *Adv Funct Mater*. 2019;29(28):1901336.

118. Guo X, Zhang W, Zhang J, et al. Boosting sodium storage in two-dimensional phosphorene/$Ti_3C_2T_x$ MXene nanoarchitectures with stable fluorinated interphase. *ACS Nano*. 2020;14(3):3651-3659.

119. Er D, Li J, Naguib M, Gogotsi Y, Shenoy VB. Ti_3C_2 MXene as a high capacity electrode material for metal (Li, Na, K, Ca) ion batteries. *ACS Appl Mater Interfaces*. 2014;6(14):11173-11179.

120. Fan K, Ying Y, Li X, Luo X, Huang H. Theoretical investigation of V_3C_2 MXene as prospective high-capacity anode material for metal-ion (Li, Na, K, and Ca) batteries. *J Phys Chem C*. 2019;123(30):18207-18214.

121. Wang Y, Liu M, Wang Z, et al. Interlayer environment engineered MXene: pre-intercalated Zn^{2+} ions as intercalants renders the modulated Li storage. *J Energy Chem*. 2022;68:306-313.

122. Lu M, Han W, Li H, et al. Tent-pitching-inspired high-valence period 3-cation pre-intercalation excels for anode of 2D titanium carbide (MXene) with high Li storage capacity. *Energy Storage Mater*. 2019;16:163-168.

123. Xu M, Lei S, Qi J, et al. Opening magnesium storage capability of two-dimensional MXene by intercalation of cationic surfactant. *ACS Nano*. 2018;12(4):3733-3740.

124. Li G, Lian S, Song F, et al. Surface chemistry and mesopore dual regulation by sulfur-promised high volumetric capacity of $Ti_3C_2T_x$ films for sodium-ion storage. *Small*. 2021;17(49):2103626.

125. Liu R, Cao W, Han D, et al. Nitrogen-doped Nb_2CT_x MXene as anode materials for lithium ion batteries. *J Alloys Compd*. 2019;793:505-511.

126. Li M, Li X, Qin G, et al. Halogenated Ti_3C_2 MXenes with electrochemically active terminals for high-performance zinc ion batteries. *ACS Nano*. 2021;15(1):1077-1085.

127. Tian Y, An Y, Feng J. Flexible and freestanding silicon/MXene composite papers for high-performance lithium-ion batteries. *ACS Appl Mater Interfaces*. 2019;11(10):10004-10011.

128. Ma Z, Zhou X, Deng W, Lei D, Liu Z. 3D porous MXene (Ti_3C_2)/reduced graphene oxide hybrid films for advanced lithium storage. *ACS Appl Mater Interfaces*. 2018;10(4):3634-3643.

129. Zhao T, Zhai P, Yang Z, et al. Self-supporting $Ti_3C_2T_x$ foam/S cathodes with high sulfur loading for high-energy-density lithium–sulfur batteries. *Nanoscale*. 2018;10(48):22954-22962.

130. Chen Z, Yang X, Qiao X, et al. Lithium-ion-engineered interlayers of V_2C MXene as advanced host for flexible sulfur cathode with enhanced rate performance. *J Phys Chem Lett*. 2020;11(3):885-890.

131. Zhong X, Wang D, Sheng J, et al. Freestanding and sandwich MXene-based cathode with suppressed lithium polysulfides shuttle for flexible lithium–sulfur batteries. *Nano Lett*. 2022;22(3):1207-1216.

132. Zhang D, Wang S, Hu R, et al. Catalytic conversion of polysulfides on single atom zinc implanted MXene toward high-rate lithium–sulfur batteries. *Adv Funct Mater*. 2020;30(30):2002471.

133. Yang S, Liu Q, Lu Q, et al. A facile strategy to improve the electrochemical performance of porous organic polymer-based lithium–sulfur batteries. *Energy Technol*. 2019;7(12):1900583.

134. Ding L, Lu Q, Permana ADC, et al. Oxygen-doped carbon nitride tubes for highly stable lithium–sulfur batteries. *Energy Technol*. 2021;9(4):2001057.

135. Feng Y, Liu H, Lu Q, et al. Designing hierarchical MnO/polypyrrole heterostructures to couple polysulfides adsorption and electrocatalysis in lithium–sulfur batteries. *J Power Sources*. 2022;520:230885.

136. Giebeler L, Balach J. MXenes in lithium–sulfur batteries: scratching the surface of a complex 2D material—a minireview. *Materials Today Commun*. 2021;27:102323.

137. Balach J, Giebeler L. MXenes and the progress of Li–S battery development—a perspective. *J Phys Energy*. 2021;3(2):021002.

138. Lee DK, Chae Y, Yun H, Ahn CW, Lee JW. CO_2-oxidized $Ti_3C_2T_x$–MXenes components for lithium–sulfur batteries: suppressing the shuttle phenomenon through physical and chemical adsorption. *ACS Nano*. 2020;14(8):9744-9754.

139. Tian Y, An Y, Wei C, et al. Flexible and free-standing $Ti_3C_2T_x$ MXene@Zn paper for dendrite-free aqueous zinc metal batteries and nonaqueous lithium metal batteries. *ACS Nano*. 2019;13(10):11676-11685.

140. Fang Y, Lian R, Li H, et al. Induction of planar sodium growth on MXene ($Ti_3C_2T_x$)-modified carbon cloth hosts for flexible sodium metal anodes. *ACS Nano*. 2020;14(7):8744-8753.

141. Wang C-Y, Zheng Z-J, Feng Y-Q, Ye H, Cao F-F, Guo Z-P. Topological design of ultrastrong MXene paper hosted Li enables ultrathin and fully flexible lithium metal batteries. *Nano Energy*. 2020;74:104817.

142. Tang X, Zhou D, Li P, et al. MXene-based dendrite-free potassium metal batteries. *Adv Mater*. 2020;32(4):1906739.

143. Jiang G, Qu C, Xu F, et al. Glassy metal–organic-framework-based quasi-solid-state electrolyte for high-performance lithium-metal batteries. *Adv Funct Mater*. 2021;31(43):2104300.

144. Xu F, Qu C, Lu Q, et al. Atomic Sn-enabled high-utilization, large-capacity, and long-life Na anode. *Sci Adv*. 2022;8(19):eabm7489.

145. Lu Q, Omar A, Hantusch M, et al. Dendrite-free and corrosion-resistant sodium metal anode for enhanced sodium batteries. *Appl Surf Sci*. 2022;600:154168.

146. Lu Q, Yang A, Omar A, et al. Recent advances in stabilization of sodium metal anode in contact with organic liquid and solid-state electrolytes. *Energy Technol*. 2022;10(7):2200149.

147. Lu Q, Wang X, Omar A, Mikhailova D. 3D Ni/Na metal anode for improved sodium metal batteries. *Mater Lett*. 2020;275:128206.

148. Ha S, Kim D, Lim H-K, Koo CM, Kim SJ, Yun YS. Lithiophilic MXene-guided lithium metal nucleation and growth behavior. *Adv Funct Mater*. 2021;31(32):2101261.

149. Luo J, Lu X, Matios E, et al. Tunable MXene-derived 1D/2D hybrid nanoarchitectures as a stable matrix for dendrite-free and ultrahigh capacity sodium metal anode. *Nano Lett*. 2020;20(10):7700-7708.

150. Tian Y, An Y, Liu C, Xiong S, Feng J, Qian Y. Reversible zinc-based anodes enabled by zincophilic antimony engineered MXene for stable and dendrite-free aqueous zinc batteries. *Energy Storage Mater*. 2021;41:343-353.

151. Mashtalir O, Lukatskaya MR, Zhao MQ, Barsoum MW, Gogotsi Y. Amine-assisted delamination of Nb_2C MXene for Li-ion energy storage devices. *Adv Mater*. 2015;27(23):3501-3506.

152. Wang Z, Yu K, Feng Y, Qi R, Ren J, Zhu Z. $VO_2(p)$-V_2C (MXene) grid structure as a lithium polysulfide catalytic host for high-performance Li–S battery. *ACS Appl Mater Interfaces*. 2019;11(47):44282-44292.

153. Jiang G, Zheng N, Chen X, et al. In-situ decoration of MOF-derived carbon on nitrogen-doped ultrathin MXene nanosheets to multifunctionalize separators for stable Li–S batteries. *Chem Eng J*. 2019;373:1309-1318.

154. An Y, Tian Y, Liu C, Xiong S, Feng J, Qian Y. Rational design of sulfur-doped three-dimensional $Ti_3C_2T_x$ MXene/ZnS heterostructure as multifunctional protective layer for dendrite-free zinc-ion batteries. *ACS Nano*. 2021;15(9):15259-15273.

155. Sun P, Liu J, Liu Q, et al. Nitrogen and sulfur co-doped MXene ink without additive for high-performance inkjet-printing micro-supercapacitors. *Chem Eng J*. 2022;450:138372.

156. Hu M, Zhang H, Hu T, Fan B, Wang X, Li Z. Emerging 2D MXenes for supercapacitors: status, challenges and prospects. *Chem Soc Rev*. 2020;49(18):6666-6693.

157. Lukatskaya MR, Kota S, Lin Z, et al. Ultra-high-rate pseudo-capacitive energy storage in two-dimensional transition metal carbides. *Nat Energy*. 2017;2(8):17105.

158. Tang J, Mathis T, Zhong X, et al. Optimizing ion pathway in titanium carbide MXene for practical high-rate supercapacitor. *Adv Energy Mater*. 2021;11(4):2003025.

159. Tian Y, Ju M, Luo Y, Bin X, Lou X, Que W. In situ oxygen doped $Ti_3C_2T_x$ MXene flexible film as supercapacitor electrode. *Chem Eng J*. 2022;446:137451.

160. Levitt AS, Alhabeb M, Hatter CB, Sarycheva A, Dion G, Gogotsi Y. Electrospun MXene/carbon nanofibers as supercapacitor electrodes. *J Mater Chem*. 2019;7(1):269-277.

161. Li Z, Dall'Agnese Y, Guo J, Huang H, Liang X, Xu S. Flexible freestanding all-MXene hybrid films with enhanced capacitive performance for powering a flex sensor. *J Mater Chem*. 2020;8(32):16649-16660.

162. Bin X, Tian Y, Luo Y, et al. High-performance flexible and free-standing N-doped $Ti_3C_2T_x$/MoO_x films as electrodes for supercapacitors. *Electrochim Acta*. 2021;389:138774.

163. Yu J, Zeng M, Zhou J, et al. A one-pot synthesis of nitrogen doped porous MXene/TiO_2 heterogeneous film for high-performance flexible energy storage. *Chem Eng J*. 2021;426:130765.

164. Zhou Y, Maleski K, Anasori B, et al. $Ti_3C_2T_x$ MXene-reduced graphene oxide composite electrodes for stretchable supercapacitors. *ACS Nano*. 2020;14(3):3576-3586.

How to cite this article: Lu Q, Liu C, Zhao Y, et al. Freestanding MXene-based macroforms for electrochemical energy storage applications. *SusMat*. 2023;3:471-497. https://doi.org/10.1002/sus2.151


AUTHOR BIOGRAPHIES

Qiongqiong Lu received his PhD degree at Technische Universität Dresden in 2022 and then conducted postdoctoral research at Leibniz Institute for Solid State and Materials Research (IFW) Dresden, Germany. He subsequently joined the Henan Academy of Sciences. His research

focuses on functional materials for electrochemical energy storage applications.

Congcong Liu is a PhD candidate at Leibniz Institute for Solid State and Materials Research (IFW) Dresden. She received her BS degree from Inner Mongolia University and MS degree from Technische Universität Dresden, Germany, in 2021. Her research interests are energy storage materials and in situ synchrotron X-ray diffraction/absorption spectroscopy analysis.
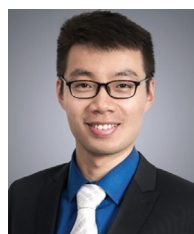
Minghao Yu received his PhD degree in Material Physics and Chemistry from Sun Yat-Sen University in June 2017. In March 2019, he became a research group leader of the Chair for Molecular Functional Materials at Technische Universität Dresden. His research interests focus on the development of advanced functional materials for applications of energy storage (supercapacitors and metal-ion batteries) and conversion (electrocatalysis and metal-air batteries).